Masthead Logo

University of Kentucky
UKnowledge

Physics and Astronomy Faculty Publications

Physics and Astronomy

12-18-2017

Spin-Valley Coherent Phases of the $\nu = 0$ Quantum Hall State in Bilayer Graphene

Ganpathy Murthy
University of Kentucky, ganpathy.murthy@uky.edu

Efrat Shimshoni
Bar-Ilan University, Israel

H. A. Fertig
Indiana University - Bloomington

Right click to open a feedback form in a new tab to let us know how this document benefits you.

Follow this and additional works at: https://uknowledge.uky.edu/physastron_facpub

Part of the Astrophysics and Astronomy Commons, and the Physics Commons

Repository Citation

Murthy, Ganpathy; Shimshoni, Efrat; and Fertig, H. A., "Spin-Valley Coherent Phases of the $\nu = 0$ Quantum Hall State in Bilayer Graphene" (2017). *Physics and Astronomy Faculty Publications*. 516.
https://uknowledge.uky.edu/physastron_facpub/516

This Article is brought to you for free and open access by the Physics and Astronomy at UKnowledge. It has been accepted for inclusion in Physics and Astronomy Faculty Publications by an authorized administrator of UKnowledge. For more information, please contact UKnowledge@lsv.uky.edu.

Spin-Valley Coherent Phases of the $\nu = 0$ Quantum Hall State in Bilayer Graphene

Notes/Citation Information
Published in *Physical Review B*, v. 96, issue 24, 245125, p. 1-21.

©2017 American Physical Society

The copyright holder has granted permission for posting the article here

Digital Object Identifier (DOI)
https://doi.org/10.1103/PhysRevB.96.245125

This article is available at UKnowledge: https://uknowledge.uky.edu/physastron_facpub/516

Spin-valley coherent phases of the $\nu = 0$ quantum Hall state in bilayer graphene

Ganpathy Murthy,[1] Efrat Shimshoni,[2] and H. A. Fertig[3]
[1]*Department of Physics and Astronomy, University of Kentucky, Lexington, Kentucky 40506-0055, USA*
[2]*Department of Physics, Bar-Ilan University, Ramat-Gan 52900, Israel*
[3]*Department of Physics, Indiana University, Bloomington, Indiana 47405, USA*
(Received 18 September 2017; published 18 December 2017)

Bilayer graphene (BLG) offers a rich platform for broken-symmetry states stabilized by interactions. In this work, we study the phase diagram of BLG in the quantum Hall regime at filling factor $\nu = 0$ within the Hartree-Fock approximation. In the simplest noninteracting situation, this system has eight (nearly) degenerate Landau levels near the Fermi energy, characterized by spin, valley, and orbital quantum numbers. We incorporate in our study two effects not previously considered: (i) the nonperturbative effect of trigonal warping in the single-particle Hamiltonian, and (ii) short-range SU(4) symmetry-breaking interactions that distinguish the energetics of the orbitals. We find within this model a rich set of phases, including ferromagnetic, layer polarized, canted antiferromagnetic, Kekule, a "spin-valley entangled" state, and a "broken U(1) × U(1)" phase. This last phase involves independent spontaneous symmetry breaking in the layer and valley degrees of freedom, and has not been previously identified. We present phase diagrams as a function of interlayer bias D and perpendicular magnetic field $B_\perp$ for various interaction and Zeeman couplings, and discuss which are likely to be relevant to BLG in recent measurements. Experimental properties of the various phases and transitions among them are also discussed.

DOI: 10.1103/PhysRevB.96.245125

I. INTRODUCTION

Two-dimensional systems with discrete degrees of freedom in the quantum Hall regime support a variety of possible broken-symmetry states, a phenomenon known as quantum Hall ferromagnetism (QHF) [1]. In this context, graphene has presented itself as a particularly exciting system, both in its monolayer and bilayer forms. These systems differ from more conventional two-dimensional electron gases in supporting a $\nu = 0$ quantized Hall effect, a consequence of negative energy levels that are necessarily present in their noninteracting spectra [2,3]. Moreover, the presence of nearly degenerate Landau levels (arising from internal degrees of freedom such as spin, valley, and layer) near the Fermi energy in undoped systems suggests that these systems offer a unique platform for QHF physics [4].

In this work, we study QHF in bilayer graphene (BLG) subject to magnetic and electric fields. In zero magnetic field, working in the tight-binding model with nearest-neighbor hoppings only, the system distinguishes itself from single-layer graphene at the noninteracting level in supporting two quadratic band-touching (QBT) points, at the K and K' points in the Brillouin zone, in contrast with monolayer graphene which supports Dirac points at these locations. When undoped, the Fermi energy passes through these QBT's, opening the possibility of many-body instabilities when interactions are included in zero magnetic field [5–8] . In the presence of a field, this system supports eight Landau levels near the Fermi energy, offering a particularly rich set of possibilities for ground states with broken symmetries. These levels arise from spin and valley quantum numbers, as well as orbital states $n = 0, 1$ which are degenerate at any magnetic field in the simplest models, when no electric field $D_\perp$ is applied perpendicular to the system.

Previous studies of this system have focused on models which differ in their choice of physical effects retained in the single-particle Hamiltonian, and in how interactions are modeled. Projection of the long-range Coulomb interaction into this eightfold manifold yields an effective Hamiltonian with a layer-polarized state at large $D_\perp$ and a ferromagnetic state at small $D_\perp$, with a first-order transition separating them [9,10]. Distinguishing intralayer and interlayer Coulomb interactions, as well as inclusion of particle-hole symmetry-breaking terms, leads to the appearance of a state spontaneously breaking a U(1) symmetry [11–14].

Interactions in general are, however, more complicated than the long-range Coulomb form because at the microscopic scale they may have lower symmetry (e.g., onsite Hubbard interactions). Moreover, short-range interactions have greater effect than expected based on projection directly into the small set of Landau levels near the Fermi energy because they impact the energetics of the Landau levels below them [12–19]. An effective method for dealing with this, introduced by Kharitonov [20,21], uses phenomenological short-range interactions consistent with the symmetries of the lattice, in principle incorporating renormalizations from the Landau levels deep within the Dirac sea. In this study, we adopt this general approach of effective interactions confined to the set of Landau levels near zero energy.

Experimentally, evidence for phase transitions among states of different broken symmetries has been accumulating. Two-terminal conductance experiments reveal quantized Hall states at low and high $D_\perp$ at filling factor $\nu = 0$, interrupted at intermediate $D_\perp$ scales by a region where the transport gap vanishes [22–24], indicating a phase transition between different quantized Hall states. The value of $D_\perp$ at which this transition occurs increases monotonically with increasing $B_\perp$, the magnetic field component perpendicular to the bilayer. The high-$D_\perp$ phase is rather naturally identified with a layer-polarized state, while the low-$D_\perp$ phase is largely thought to represent a canted antiferromagnet (CAF) phase as was suggested in Ref. [21]. More recent capacitance measurements [25], however, show signatures of a separate intermediate gapped phase between the low- and high-$D_\perp$ limits, appearing

 ©2017 American Physical Society

above $B_\perp \sim 12$–13 T. Finally, in some samples the region in $D_\perp$ separating the low- and high-$D_\perp$ states even at lower $B_\perp$ is not perfectly sharp, raising the possibility of other phases existing in the transition region [24,26].

In this work, we explore the phase diagram of bilayer graphene at $\nu = 0$ using a model of the form introduced in Ref. [21], within the Hartree-Fock approximation. Our model incorporates two ingredients which, to our knowledge, have not been considered before in the context of interacting BLG. The first is the nonperturbative inclusion of "trigonal warping" [3] (arising from a hopping amplitude t_3 between sites in different layers which are not above one another) in the single-particle states comprising the low-energy manifold. (Here and in the following, by "low-energy manifold" we will mean the states lying near the Fermi energy). The t_3 term is allowed by the spatial symmetries of the lattice, and generically arises in *ab initio* approaches to the band structure of BLG (see Ref. [27] and references therein). This hopping term significantly distorts the QBT in zero field, replacing it with four Dirac points [3]. From a renormalization group (RG) perspective, recent work [28] has shown that the t_3 term, being allowed by symmetry, is generated by short-range interactions, even if it is assumed to be zero in the bare theory. Once generated, it is relevant, and flows to large values at low energies. In large magnetic fields, this term has a very small effect [3]. In consequence, this term has previously been either neglected [11,12,14,21] or taken into account only perturbatively [13]. We find, however, that for experimentally relevant values of $B_\perp$, the nonperturbative effect of the t_3 term is crucial to stabilizing hitherto unknown broken-symmetry states.

The second crucial element in our theory is the inclusion of short-range interactions not included in Ref. [21]: a density-density coupling g_0, and an orbital anisotropy coupling g_{nz}, an Ising-type interaction energy for fluctuations in the density differences between the two spatial orbitals. Both these couplings are allowed by symmetry, and we find that including them yields a minimal model with a phase diagram qualitatively consistent with current experimental observations.

The phases that we find to be stable in different parameter regimes include (1) a fully layer-polarized (FLP) state, (2) a fully spin-polarized (ferromagnetic, FM) state; (3) a canted antiferromagnetic state (CAF), characterized by partial spin alignment along the direction of the total magnetic field and antiferromagnetic alignment between electrons in different valleys; (4) a Kekule state (KEK), which may be regarded as an analog of the CAF in which the roles of spin and valley degrees of freedom have been interchanged; (5) a "spin-valley entangled" (SVE) state, in which the occupied single-particle states involve coherent superpositions of states of opposing spin and valley index, similar to the spin-layer coherent state of Refs. [11,13]; (6) a partial orbitally polarized (POP) state; and finally (7) a more exotic "broken U(1) × U(1)" state, which supports nontrivial coherence among different combinations of the single-particle states in the spin-valley manifold such that two different U(1) symmetries are spontaneously broken. This contrasts with the other coherent states that we find (which have been discussed in earlier literature as well [11–14,21]), the CAF, KEK, and SVE, which represent families of states with a single spontaneously broken U(1) symmetry.

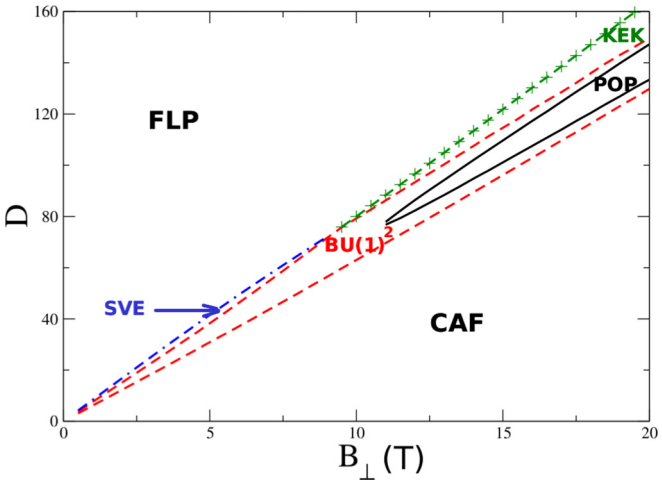

FIG. 1. The theoretical phase diagram in the tuning parameters $B_\perp$ and the perpendicular electric field (labeled D in the figure and proportional to $D_\perp$) of our model in a range of assumed couplings which exhibits the broken U(1) × U(1) [BU(1)^2] state. Here and in all the figures following, $B_\perp$ is in Tesla, and D is in arbitrary units. The boundaries of the BU(1)^2 state are the dashed red lines, while the boundaries of the partially orbitally polarized (POP) state are the solid black lines. The blue dashed-dotted line is the upper boundary of the spin-valley entangled (SVE) phase, while the green dashed line with the + symbols is the upper boundary of the Kekule (KEK) state. The canted antiferromagnet (CAF) occupies the small D part of the diagram at all values of $B_\perp$. For small values of $B_\perp \leq 11$ T, as one increases D starting from zero, one successively encounters the CAF state, the BU(1)^2 state, the spin-valley-entangled (SVE) state, and finally, at large values of D, the fully layer-polarized (FLP) state. At larger values of $B_\perp > 11$ T, again starting from $D = 0$, one encounters the CAF, the BU(1)^2 state, the partially orbitally polarized (POP) state, the Kekule (KEK) state, and finally the FLP state. All solid lines indicate first-order phase transitions while the broken lines indicate second-order transitions.

To our knowledge, the existence of a broken U(1) × U(1) [BU(1)^2] phase has not been predicted in previous studies of the phase diagram, although hints of it have been seen even at $t_3 = 0$ [29]: in that case, a BU(1)^2 state supporting collective modes with vanishing energy was identified at the CAF/FM to KEK/FLP phase boundary (we explain this connection in Secs. IV C 3, IV D, and V B). Within our model, the BU(1)^2 phase requires a nonzero trigonal warping in the single-particle Hamiltonian, as well as the g_0 and g_{nz} couplings. We find that for physically reasonable sets of parameters, it connects states with fewer broken symmetries, such as the CAF and KEK, as the interlayer potential $D_\perp$ or the perpendicular field $B_\perp$ increases. Each of the two U(1) angles involved comes with a stiffness, one or the other of which vanishes continuously as the transition to another state is approached. This suggests the possibility of thermal or quantum disordering of the phase, and the possibility that the state does not manifest the quantized Hall effect at experimentally relevant temperatures. If so, this would introduce a broad transition region between, for example, CAF and FLP states as a function of $D_\perp$, rather than a sharp transition between them as would occur in a first-order transition. A typical phase diagram is illustrated in Fig. 1.

The rest of this paper is organized as follows. In Sec. II, we introduce the noninteracting Hamiltonian for BLG and the low-energy basis states we will be using. These basis states include the effect of the trigonal warping nonperturbatively. In Sec. III, we will introduce the interacting Hamiltonian, and present the general formula for the energy of a Hartree-Fock (HF) state. In Sec. IV, we describe the states that are encountered in our numerical calculation. We also present the linear instabilities of these states which helps us identify various second-order phase transitions. Most importantly, it helps us identify three different regimes of the coupling constants which result in different topologies of the phase diagram. In Sec. V, we present a brief analysis of the possible phase diagrams at small $B_\perp$ and large $B_\perp$. This distinction arises because the term in the Hamiltonian induced by the trigonal warping scales as $\sqrt{B_\perp}$, whereas other terms are proportional to $B_\perp$. Section V also contains our main results. These include phase diagrams in $B_\perp - D$ space (D is proportional to the perpendicular electric field applied on the sample) for three different regimes of coupling constants that produce different topologies for the phase diagrams. Section VI includes a discussion of experimental consequences relevant to our phase diagrams, and notes a few limitations of our analysis. Section VII concludes with a summary, open questions, and future directions.

II. NONINTERACTING HAMILTONIAN AND LOW-ENERGY STATES

To set our notation from the start, we will use the index $n = 0,1$ for the orbital degree of freedom, the Greek indices $\alpha = 0,1$ for the valley (where $\alpha,\beta = 0 \equiv K$ and $\alpha,\beta = 1 \equiv K'$), and the indices $s,s' = 0,1$ for spin ($s = 0 \equiv\uparrow$, and $s = 1 \equiv\downarrow$). As a starting point for analyzing the single-body part of the Hamiltonian we consider a Bernal stacked BLG, where the A site of one layer is directly on top of the B′ site of the other. In the presence of a perpendicular electric field $D_\perp$ and a magnetic field $\mathbf{B}$ (introduced via a gauge choice where $A_y = B_\perp x$), the approximate effective Hamiltonian describing electron states on the remaining two sites of the BLG unit cell is given (for valley $\mathbf{K}$, spin $s = 0,1 =\uparrow, \downarrow$ and wave vector k in the $\hat{y}$ direction) by [3,27]

$$\begin{aligned} H_{\rm eff}^{Ks} &= H_0 + H_Z + H_D, \\ H_0 &= -\hbar\omega_c \begin{pmatrix} -\tilde{\epsilon}_a a^\dagger a & \left(a^\dagger\right)^2 + \lambda a \\ (a)^2 + \lambda a^\dagger & -\tilde{\epsilon}_a a a^\dagger \end{pmatrix}, \\ H_Z &= -\begin{pmatrix} E_z(-1)^s & 0 \\ 0 & E_z(-1)^s \end{pmatrix}, \\ H_D &= -\begin{pmatrix} D & 0 \\ 0 & -D \end{pmatrix}. \end{aligned} \tag{1}$$

Here, $E_z \propto |\mathbf{B}|$ is the Zeeman energy, $D \propto D_\perp$ is (half) the interlayer bias, and $a = \frac{\ell}{\sqrt{2}}[\partial_x + (x - X)/\ell^2]$ is the Landau level lowering operator (with $\ell = \sqrt{\hbar c/eB_\perp}$ the magnetic length and $X = k\ell^2$ the guiding center coordinate). The parameters of H_0 account for all the tight-binding parameters listed in Ref. [27], including the longer-range interlayer hopping coefficients t_3, t_4 and a particle-hole breaking onsite energy Δ:

$$\begin{aligned} \omega_c &= \frac{\hbar}{\ell^2 m} \sim B_\perp, \\ m &\equiv \frac{t_1^2 - \Delta^2}{2\left[t_1\left(v_\perp^2 + v_4^2\right) + 2v_\perp v_4 \Delta\right]} \approx \frac{t_1}{2v_\perp^2}, \end{aligned} \tag{2}$$

where $v_\perp = \sqrt{3}|t_\perp|a_0/2\hbar$, $v_4 = \sqrt{3}|t_4|a_0/2\hbar$ with $t_\perp$ the interlayer hopping obeying $|t_\perp| \gg |t_4|,|t_1| \gg \Delta$. The dimensionless parameter

$$\tilde{\epsilon}_a = \frac{\left[\Delta\left(v_\perp^2 + v_4^2\right) + 2t_1 v_\perp v_4\right]}{\left[t_1\left(v_\perp^2 + v_4^2\right) + 2v_\perp v_4 \Delta\right]} \approx \frac{\Delta}{t_1} \tag{3}$$

determines the orbital anisotropy energy, and is independent of $B_\perp$, whereas

$$\lambda = \frac{\sqrt{2}v_3 m\ell}{\hbar} = \frac{\sqrt{3/2}|t_3|a_0 m\ell}{\hbar^2} \sim \frac{1}{\sqrt{B_\perp}}. \tag{4}$$

Finally, $H_{\rm eff}^{K's}$ (for the other valley $\mathbf{K'}$) can be obtained from Eq. (1) by trading $a^\dagger \leftrightarrow a$, $D \leftrightarrow -D$, and $\lambda \leftrightarrow -\lambda$.

The spectrum and eigenstates of the above effective Hamiltonian are well known for the case $\lambda = \tilde{\epsilon}_a = 0$, i.e., when subleading hopping parameters are neglected. In particular, there is a twofold orbitally degenerate manifold of zero-energy eigenstates of H_0 (ignoring spin and the guiding center indices for the moment):

$$|n,K\rangle = \begin{pmatrix} |n\rangle \\ 0 \end{pmatrix}, \quad |n,K'\rangle = \begin{pmatrix} 0 \\ |n\rangle \end{pmatrix}, \tag{5}$$

where $|n\rangle$ with $n = 0,1$ are Landau level (LL) wave functions. Their corresponding energies are $\epsilon_{n,\alpha,s} = -D(-1)^\alpha - E_z(-1)^s$. Note that the twofold degeneracy of $n = 0,1$ can be traced back to the quadratic band-touching (QBT) characteristic to BLG. Adding a finite $\tilde{\epsilon}_a$ to H_0 [Eq. (1)] maintains the eigenstates [Eq. (5)], and merely lifts the degeneracy of the $n = 0,1$ orbitals by a small asymmetry energy. However, the parameter λ associated with the t_3-hopping term, which introduces trigonal warping of the QBT, fundamentally changes the structure of the electronic states. Moreover, using empirical estimates of the bare parameters [27,30] in Eq. (4), one obtains $\lambda \equiv \lambda_1/\sqrt{B_\perp}$ where $B_\perp$ is in Tesla and $\lambda_1 \sim 1$ is the value of λ at $B_\perp = 1$ T. This implies that its effect is not necessarily perturbative; its relative significance is tunable with $B_\perp$, and becomes especially pronounced for moderately low fields of the order of a Tesla. Indeed, as we show below, the resulting change in the structure of noninteracting electron states has dramatic consequences for the nature of broken-symmetry states when interactions are included.

We therefore focus on the case where $\lambda \neq 0$ is arbitrary, and $\tilde{\epsilon}_a = 0$ (corrections due to a finite $\tilde{\epsilon}_a$ will be accounted for later on as a perturbation). The eigenstates of $H_{\rm eff}^{Ks}$, $H_{\rm eff}^{K's}$ can then be cast as (again ignoring spin and guiding center indices)

$$|K\rangle = \begin{pmatrix} |\psi_K\rangle \\ 0 \end{pmatrix}, \quad |K'\rangle = \begin{pmatrix} 0 \\ |\psi_{K'}\rangle \end{pmatrix}, \tag{6}$$

$$\text{where} \quad (a^2 + (-1)^\alpha \lambda a^\dagger)|\psi_\alpha\rangle = 0.$$

Using the operator identity $[a, f(a^\dagger)] = f'(a^\dagger)$ [with $f(x)$ an analytic function], Eq. (6) can be cast as an operator version

of the Airy equation $y'' - xy = 0$ whose solutions are the functions [31] Ai(x), Bi(x). Employing their integral form, we obtain the following basis for the states $|\psi_K\rangle$ (i.e., for $\alpha = 0$ and $\lambda > 0$):

$$|\psi_A, K\rangle = \int_0^\infty dt \left[\cos\left(\frac{t^3}{3\lambda} - ta^\dagger\right)\right]|0\rangle,$$
$$|\psi_B, K\rangle = \int_0^\infty dt \left[e^{-\frac{t^3}{3\lambda} - ta^\dagger} + \sin\left(\frac{t^3}{3\lambda} - ta^\dagger\right)\right]|0\rangle. \tag{7}$$

It is convenient to express these integral forms as power series in λ. This yields $|\psi_A\rangle$, $|\psi_B\rangle$ as linear combinations of the orthonormal orbital states (see Appendix A)

$$|\psi_0, K\rangle = \sum_{m=0}^\infty A_{0m}|3m\rangle,$$
$$A_{0m} \equiv C_0(-1)^m \frac{(3\lambda)^m}{\sqrt{(3m)!}} \frac{\Gamma\left(m + \frac{1}{3}\right)}{\Gamma\left(\frac{1}{3}\right)};$$
$$|\psi_1, K\rangle = \sum_{m=0}^\infty A_{1m}|3m+1\rangle,$$
$$A_{1m} \equiv C_1(-1)^m \frac{(3\lambda)^m}{\sqrt{(3m+1)!}} \frac{\Gamma\left(m + \frac{2}{3}\right)}{\Gamma\left(\frac{2}{3}\right)}, \tag{8}$$

where $|N\rangle = \frac{1}{\sqrt{N!}}(a^\dagger)^N|0\rangle$ are the LL states and the normalization factors C_n guarantee $\sum_0^\infty A_{nm}^2 = 1$. Recalling Eq. (6), the solutions for the wave function $|\psi_{K'}\rangle$ are directly obtained from Eq. (8) by the substitution $\lambda \to -\lambda$. For convenience, we recall our label α for the valleys such that $\alpha = K = 0$, $\alpha = K' = 1$, and the corresponding orbital labels $n = 0, 1$, so that

$$|n,\alpha\rangle \equiv \sum_{m=0}^\infty (-1)^{m\alpha} A_{nm}|3m+n\rangle. \tag{9}$$

The eigenstates of the effective Hamiltonian [with $\tilde{\epsilon}_\alpha = 0$ in Eq. (1)] are then given by

$$|0,K,s\rangle = \begin{pmatrix} |0,0,s\rangle \\ 0 \end{pmatrix}, \quad |1,K,s\rangle = \begin{pmatrix} |1,0,s\rangle \\ 0 \end{pmatrix},$$
$$|0,K',s\rangle = \begin{pmatrix} 0 \\ |0,1,s\rangle \end{pmatrix}, \quad |1,K',s\rangle = \begin{pmatrix} 0 \\ |1,1,s\rangle \end{pmatrix}, \tag{10}$$

where the explicit dependence on the parameter λ is given in Eqs. (8) and (9) and the states $|n,\alpha,s\rangle \equiv |n,\alpha\rangle \otimes |s\rangle$ incorporate spin. Note that the wave vector k, or equivalently the guiding center $X = k\ell^2$, is also a quantum number of the states, but is suppressed in the above expressions.

This basis of low-energy states, i.e., states close to the Fermi energy, has the full nonperturbative dependence on t_3 which will turn out to be important for the rest of our analysis.

To evaluate the energy spectrum, we consider the full effective Hamiltonian where the anisotropy parameter $\tilde{\epsilon}_a$ in Eq. (1) is finite but small [see Eq. (3)], so that the corresponding terms can be treated perturbatively. Using the matrix elements

$$\langle 0,\alpha|a^\dagger a|0,\alpha\rangle = \sum_{m=0}^\infty 3m|A_{0m}|^2,$$
$$\langle 1,\alpha|a^\dagger a|1,\alpha\rangle = \sum_{m=0}^\infty (3m+1)|A_{1m}|^2, \tag{11}$$

and implementing the substitution $D \to -D$ for $K \to K'$, we obtain the energy levels corresponding to the states (10) to first order in $\tilde{\epsilon}_\alpha$:

$$\epsilon_{0,K} = D + \tilde{\epsilon}_\alpha \sum_{m=0}^\infty 3m|A_{0m}|^2,$$
$$\epsilon_{1,K} = D + \tilde{\epsilon}_\alpha \sum_{m=0}^\infty (3m+1)|A_{1m}|^2,$$
$$\epsilon_{0,K'} = -D + \tilde{\epsilon}_\alpha \sum_{m=0}^\infty 3m|A_{0m}|^2,$$
$$\epsilon_{1,K'} = -D + \tilde{\epsilon}_\alpha \sum_{m=0}^\infty (3m+1)|A_{1m}|^2. \tag{12}$$

For each valley, this introduces an orbital anisotropy

$$\epsilon_a \equiv \epsilon_{1,\alpha} - \epsilon_{0,\alpha} = \tilde{\epsilon}_\alpha \sum_{m=0}^\infty [(3m+1)|A_{1m}|^2 - 3m|A_{0m}|^2] \tag{13}$$

which can be numerically evaluated for arbitrarily large λ using the expressions for A_{nm} [Eq. (8)].

III. INTERACTION HAMILTONIAN AND HARTREE-FOCK

As explained above, there are three discrete quantum numbers for the noninteracting single-particle states in BLG, representing spin, valley, and the $n = 0, 1$ orbitals. To begin dealing with interactions, we divide the basic Coulomb interaction into a long-range part that has the full SU(4) symmetry of spin and valley indices, and an effective short-range part. The short-range interactions (including those present at the bare level) should have SU(2) symmetry in the spin sector and a U(1) symmetry in the valley sector. There is no symmetry in the orbital sector because the $n = 0$ and 1 orbitals are different, and have no symmetry relating them. Upon the application of a Zeeman field, the symmetry of the spin sector is also reduced to U(1). Thus, the symmetry of the full Hamiltonian is $\mathrm{U(1)_{spin}} \times \mathrm{U(1)_{valley}}$.

Following previous work in single-layer graphene [20], we will assume that the relevant interactions at low energy have no explicit spin dependence. Translation invariance implies that at low energy there should be two kinds of interactions, those that transfer a momentum small compared to a reciprocal lattice vector, and those that transfer a momentum close to the intervalley momentum $\Delta\mathbf{K} = \mathbf{K} - \mathbf{K}'$. Taking all these conditions into account, we obtain a large set of possible interactions, each with its own coupling.

Such a high-dimensional coupling constant space is very hard to analyze systematically. Hence, in this work, we will simplify the system by considering a "minimal" model which contains only four distinct couplings. (i) v_0 is a short-range total-density total-density interaction, which has the full SU(4) symmetry of the Coulomb interaction, must generically be present in any model. In the monolayer, this coupling is not effective in distinguishing between different ground states because of the SU(4) symmetry, but in BLG, as we will see, it does play a role in selecting the ground state due to the different form factors of the $n = 0$ and 1 orbitals. (ii) v_z is an antiferromagnetic Ising-type interaction in the valley indices. To obtain the experimentally observed states we use $v_z > 0$, which disfavors valley-polarized states. This interaction is present in the Kharitonov model of MLG and BLG [20,21]. (iii) v_{xy} is a valley in-plane coupling. To be consistent with experiments, we use $v_{xy} < 0$, which favors states with equal superpositions of the two valleys. This coupling is also present in the Kharitonov model for MLG and BLG [20,21]. (iv) v_{nz} is an Ising-type antiferromagnetic interaction in the orbital indices, and disfavors orbitally polarized states. This coupling controls the $B_\perp$ at which the partially orbitally polarized state appears [25].

Defining $c_{n\alpha sk}$ as the destruction operator for a particle in a $|n,\alpha,s,k\rangle$ state (here k is the Landau guiding center label), our minimal interaction Hamiltonian takes the form

$$\begin{aligned} H_{\rm int} = \frac{1}{2L_xL_y}\sum_{k_1,k_2,\mathbf{q}} e^{-iq_x(k_1-k_2-q_y)\ell^2} \\ \times\Bigg(v_0(\mathbf{q}) \sum_{n_im_i\alpha\beta s_1s_2} \tilde\rho^{\alpha\alpha}_{n_1n_2}(\mathbf{q})\tilde\rho^{\beta\beta}_{m_1m_2}(-\mathbf{q}) : c^\dagger_{n_1\alpha s_1,k_1-q_y} c_{n_2\alpha s_1,k_1} c^\dagger_{m_1\beta s_2,k_2+q_y} c_{m_2\beta s_2,k_2} : \\ + v_z(\mathbf{q}) \sum_{n_im_i\alpha\beta s_1s_2} \tilde\rho^{\alpha\alpha}_{n_1n_2}(\mathbf{q})\tilde\rho^{\beta\beta}_{m_1m_2}(-\mathbf{q}) : c^\dagger_{n_1\alpha s_1,k_1-q_y} \tau_z c_{n_2\alpha s_1,k_1} c^\dagger_{m_1\beta s_2,k_2+q_y} \tau_z c_{m_2\beta s_2,k_2} : \\ + 2v_{xy}(\mathbf{q}) \sum_{n_im_is_1s_2} \tilde\rho^{KK'}_{n_1n_2}(\mathbf{q})\tilde\rho^{K'K}_{m_1m_2}(-\mathbf{q}) : c^\dagger_{n_1Ks_1,k_1-q_y} c_{n_2K's_1,k_1} c^\dagger_{m_1K's_2,k_2+q_y} c_{m_2Ks_2,k_2} : \\ + v_{nz}(\mathbf{q}) \sum_{n_1n_2\alpha\beta s_1s_2} (-1)^{n_1+n_2}\tilde\rho^{\alpha\alpha}_{n_1n_1}(\mathbf{q})\tilde\rho^{\beta\beta}_{n_2n_2}(-\mathbf{q}) : c^\dagger_{n_1\alpha s_1,k_1-q_y} c_{n_1\alpha s_1,k_1} c^\dagger_{n_2\beta s_2,k_2+q_y} c_{n_2\beta s_2,k_2} : \Bigg). \end{aligned} \tag{14}$$

The matrix elements of the density $\tilde\rho^{\alpha\beta}_{n_1n_2}$ are defined using the states of Eq. (9) (with spin still suppressed but the guiding center indices now explicit) as

$$\langle n_1\alpha k_1|e^{-i\mathbf{q}\cdot\mathbf{x}}|n_2\beta k_2\rangle = \delta_{k_1,k_2-q_y} e^{-iq_x(k_1-q_y/2)}\tilde\rho^{\alpha\beta}_{n_1n_2}(\mathbf{q}). \tag{15}$$

Some details about these matrix elements that are relevant to our study are provided in Appendix B. The couplings v_z, v_{xy} were originally introduced by Kharitonov for monolayer graphene [20], and have exactly the same meaning here as in the monolayer. In earlier work on the edge states of monolayer graphene [32,33], we introduced the coupling v_0, which treats all the discrete labels equally and endows the system with a spin stiffness for spatial variations of the order parameter. The new coupling we introduce is v_{nz}, which is analogous to v_z, but in the orbital sector.

To proceed, one must specify forms for $v_0(\mathbf{q})$, $v_z(\mathbf{q})$, $v_{xy}(\mathbf{q})$, and $v_{nz}(\mathbf{q})$. We make the simplest possible choices, that they are constants independent of $\mathbf{q}$. This means the interactions are very short ranged in space. We note that in the case of single-layer graphene v_0 does not alter the relative energies of the various possible bulk states. However, as we will see shortly, in bilayer graphene v_0 enters the energies of different states with different coefficients, and hence plays a role in picking the true ground state.

The full effective Hamiltonian of our system truncated to the low-energy space is $H_0 + H_{\rm int}$ where

$$H_0 = -\sum_{n\alpha sk} c^\dagger_{n\alpha sk} c_{n\alpha sk}[(-1)^n\epsilon_a + (-1)^s E_Z + (-1)^\alpha D]. \tag{16}$$

Any Hartree-Fock (HF) state is fully determined by its one-body averages $\langle c^\dagger_i c_j\rangle$. We only consider states in the bulk that conserve the guiding center label k: thus, the only possible translation symmetry breaking could arise via densities with momenta $\mathbf{K} - \mathbf{K}'$. We define the matrix $\Delta^{\alpha\beta}_{mn;ss'}$ via

$$\langle{\rm HF}|c^\dagger_{m\alpha sk} c_{n\beta s'k'}|{\rm HF}\rangle \equiv \delta_{kk'}\Delta^{\alpha\beta}_{mn;ss'}, \tag{17}$$

where $|{\rm HF}\rangle$ is a Hartree-Fock state. Note that Δ is independent of k. Now, consider evaluating the average of $H_{\rm int}$ in such a state. A generic term is a sum of direct and exchange contributions, i.e.,

$$\langle{\rm HF}|c^\dagger_{n_1\alpha s_1,k_1-q_y} c^\dagger_{m_1\eta s_2,k_2+q_y} c_{m_2\gamma s_2,k_2} c_{n_2\beta s_1,k_1}|{\rm HF}\rangle = \delta_{q_y,0}\Delta^{\alpha\beta}_{n_1n_2;s_1s_1}\Delta^{\eta\gamma}_{m_1m_2;s_2s_2} - \delta_{k_1,k_2+q_y}\Delta^{\alpha\gamma}_{n_1m_2;s_1s_2}\Delta^{\eta\beta}_{m_1n_2;s_2s_1}. \tag{18}$$

The direct terms are easy to deal with because $\tilde\rho^{\alpha\beta}_{n_1n_2}(\mathbf{q}=0) = \delta_{n_1n_2}\delta_{\alpha\beta}$. The exchange integrals are a bit more involved. In Appendix B, we show the following important result, which is relevant because of our assumption that all interactions $v_i(\mathbf{q})$ are

constants v_i:

$$\int \frac{d^2q}{(2\pi)^2}\tilde{\rho}^{\alpha\beta}_{n_1n_2}(\mathbf{q})\tilde{\rho}^{\eta\gamma}_{m_1m_2}(-\mathbf{q}) = \frac{\delta_{n_1m_2}\delta_{m_1n_2}}{2\pi\ell^2} r^{(n_1)}_{\alpha\gamma} r^{(n_2)}_{\beta\eta},$$
$$r^{(n)}_{\alpha\beta} = \sum_{j=0}^{\infty}(-1)^{j(\alpha+\beta)}|A_{nj}|^2 = \begin{Bmatrix} 1 & \alpha=\beta \\ r & \alpha\neq\beta \end{Bmatrix}, \tag{19}$$
$$\text{where} \quad r = \sum_{k=0}^{\infty}(-1)^k A^2_{nk}.$$

The number r is independent of the orbital index n (see Appendix B) but does depend on $B_\perp$ via the coefficient λ [Eqs. (4) and (8)] arising originally from the trigonal warping term t_3. The most important consequence of this relation is that only Δ's diagonal in the n labels appear in the energy. Using the general reasoning of Ref. [34], since the interorbital exchange (zero here) is smaller than the intraorbital exchange, this falls into the Ising anisotropy class: the system cannot lower its energy by superposing different orbitals in a single-particle state. Operationally, this leads to the enormous simplification that we need to consider only forms of Δ which are block diagonal in n:

$$\Delta^{\alpha\beta}_{n_1n_2;s_1s_2} \equiv \delta_{n_1n_2}\Delta^{\alpha\beta}_{n_1;s_1s_2}. \tag{20}$$

Let us now define the couplings $g_i = \frac{v_i}{2\pi\ell^2}$, and the number of flux quanta passing through the sample $N_\phi = \frac{L_xL_y}{2\pi\ell^2}$. Recalling the indexing of Sec. II ($\alpha = 0$ for the K valley and 1 for the K' valley, $s = 0$ for spin up and 1 for spin down), the HF energy may then be written compactly as

$$\begin{aligned}\frac{\mathcal{E}(\{\Delta\})}{N_\phi} \equiv \tilde{\mathcal{E}}(\{\Delta\}) = &-\sum_{n\alpha s}[\epsilon_a(-1)^n + E_z(-1)^s + D(-1)^\alpha]\Delta^{\alpha\alpha}_{n;ss} \\ &+ \frac{g_0}{2}\left[\left(\sum_{n\alpha s}\Delta^{\alpha\alpha}_{n;ss}\right)^2 - \sum_{\alpha\beta ss'} r^2_{\alpha\beta}\left(\sum_n \Delta^{\alpha\beta}_{n;ss'}\right)\left(\sum_{n'}\Delta^{\beta\alpha}_{n';s's}\right)\right] \\ &+ \frac{g_z}{2}\left[\left(\sum_{n\alpha s}(-1)^n\Delta^{\alpha\alpha}_{n;ss}\right)^2 - \sum_{\alpha\beta ss'} r^2_{\alpha\beta}(-1)^{\alpha+\beta}\left(\sum_n \Delta^{\alpha\beta}_{n;ss'}\right)\left(\sum_{n'}\Delta^{\beta\alpha}_{n';s's}\right)\right] \\ &+ g_{xy}\left[r^2\left|\sum_{ns}\Delta^{KK'}_{n;ss}\right|^2 - \sum_{ss'}\left(\sum_n \Delta^{KK}_{n;ss'}\right)\left(\sum_{n'}\Delta^{K'K'}_{n',s's}\right)\right] \\ &+ \frac{g_{nz}}{2}\left[\left(\sum_{n\alpha s}(-1)^n\Delta^{\alpha\alpha}_{n:ss}\right)^2 - \sum_{nss'\alpha\beta} r^2_{\alpha\beta}\Delta^{\alpha\beta}_{n:ss'}\Delta^{\beta\alpha}_{n:s's}\right].\end{aligned} \tag{21}$$

IV. HARTREE-FOCK STATES AND LINEAR INSTABILITIES

Before we present the numerical results, let us explore the nature of the states we will encounter, parametrize them analytically, and find critical values of D at which one kind of state is unstable to another. At $\nu = 0$ four single-particle states must be filled at each guiding center. All the states we consider are one of three types. (i) All four occupied states could be in the same ($n = 0$) orbital, which would be a maximally orbitally anisotropic (MOA) state. (ii) Three of the occupied states could be in the $n = 0$ orbital while one is in the $n = 1$ orbital, a partially orbitally polarized (POP) state. (iii) Both the $n = 0$, 1 orbitals support two occupied states. In this case, the most natural choice is $\Delta^{\alpha\beta}_{0:ss'} = \Delta^{\alpha\beta}_{1:ss'}$, a state symmetric in the orbital label. We will analyze each of these possibilities in turn. In the following, when we represent Δ_0 and Δ_1 as 4×4 matrices, our ordering will be $K\uparrow$, $K\downarrow$, $K'\uparrow$, $K'\downarrow$. We will be guided by experiment in choosing our parameters; in particular, we will consider only $g_{xy} < 0$ because of the evidence that a canted antiferromagnet (CAF) state is stable in BLG, determining the sign of g_{xy}.

A. Maximally orbitally anisotropic state

This state is particularly simple. The Δ matrices are

$$\Delta_0 = 1_{4\times4}, \quad \Delta_1 = 0_{4\times4}. \tag{22}$$

This state has orbital polarization, but no valley or spin polarization. The HF energy is

$$\tilde{\mathcal{E}}_{\text{MOA}} = -4\epsilon_a + 6g_0 - 2g_z + 6g_{nz}. \tag{23}$$

We find, for our choices of parameters, that this state is never the ground state.

B. Partially orbitally polarized states

This state can be characterized by two different single-particle states in the spin-valley sector, which for the moment we generically label $|a\rangle$ and $|b\rangle$. The Δ matrices can be described as

$$\Delta_0 = 1_{4\times4} - |a\rangle\langle a|, \quad \Delta_1 = |b\rangle\langle b|. \tag{24}$$

In principle, the states $|a\rangle$, $|b\rangle$ can be arbitrary, but at the HF minimum we find them to be parametrized by a single angle θ:

$$|a\rangle = [0 \quad 0 \quad -\sin(\theta/2) \quad \cos(\theta/2)]^T, \tag{25}$$

$$|b\rangle = [\cos(\theta/2) \quad -\sin(\theta/2) \quad 0 \quad 0]^T, \tag{26}$$

where $\cos(\theta) = \frac{E_Z}{|g_{xy}|}$ for $E_Z < |g_{xy}|$ and $\cos(\theta) = 1$ for $E_Z > |g_{xy}|$. The energy of this state is

$$\tilde{\mathcal{E}}_{\rm POP} = -2\epsilon_a - 2D + 5g_0 - g_z + |g_{xy}| - \frac{E_Z^2}{|g_{xy}|} \qquad E_Z < |g_{xy}| \tag{27}$$

$$\tilde{\mathcal{E}}_{\rm POP} = -2\epsilon_a - 2D - 2E_Z + 5g_0 - g_z + 2|g_{xy}| \qquad E_Z > |g_{xy}|. \tag{28}$$

Note that the POP states have an orbital polarization of 2, a valley polarization of 2, and variable spin polarization which can never exceed 2. They also spontaneously break the U(1) spin-rotation symmetry around the direction of **B** for $E_Z < |g_{xy}|$.

C. States symmetric in orbitals

This class exhibits the richest set of HF states, and contains the following: (i) The canted antiferromagnet (CAF) which spontaneously breaks the U(1) spin-rotation symmetry around the direction of the total field **B**. The fully spin-polarized ferromagnet (FM) is a limit of the CAF. (ii) The Kekule state (KEK) which is a spin singlet but is canted in the valley sector and thus spontaneously breaks the valley U(1) symmetry. The fully layer-polarized (FLP) state is a limit of the Kekule state. (iii) A spin-valley-entangled (SVE) state that entangles $K\downarrow$ with $K'\uparrow$. (iv) A new state which is canted in both the spin and valley sectors, and thus has two distinct spontaneously broken U(1) symmetries. We will call this state the broken U(1) $\times$ U(1), or BU(1)^2 state.

It will prove convenient to look at the 4×4 matrix $\Delta_0 = \Delta_1 = \Delta$ rather than the occupied states themselves. In all the orbitally symmetric states g_{nz} only appears via the combination $g_0 + \frac{1}{2}g_{nz}$. For future convenience, we define

$$G_0 = g_0 + \tfrac{1}{2}g_{nz}, \tag{29}$$

$$\tilde{D} = (1 - r^2)G_0 + (1 + r^2)g_z + |g_{xy}|. \tag{30}$$

1. Canted antiferromagnet (CAF) and ferromagnet (FM)

These states have a Δ matrix of the form

$$\Delta = \frac{1}{2}\begin{pmatrix} 1+\cos\theta & \sin\theta & 0 & 0 \\ \sin\theta & 1-\cos\theta & 0 & 0 \\ 0 & 0 & 1+\cos\theta & -\sin\theta \\ 0 & 0 & -\sin\theta & 1-\cos\theta \end{pmatrix}. \tag{31}$$

The minimum occurs at $\cos\theta = \frac{E_Z}{2|g_{xy}|}$ for $E_z \leqslant 2|g_{xy}|$ and $\cos\theta = 1$ for $E_z > 2|g_{xy}|$. The energy is

$$\tilde{\mathcal{E}}_{\rm CAF} = 8g_0 - 4G_0 - 4g_z - \frac{E_Z^2}{|g_{xy}|}, \quad E_Z \leqslant 2|g_{xy}| \tag{32}$$

$$\tilde{\mathcal{E}}_{\rm FM} = 8g_0 - 4G_0 - 4g_z - 4E_Z + 4|g_{xy}|, \quad E_Z > 2|g_{xy}|. \tag{33}$$

The case $E_Z > 2|g_{xy}|$ corresponds to the fully spin-polarized FM state. The CAF/FM state has only spin polarization, and no orbital or valley polarization. The CAF state spontaneously breaks the U(1) spin-rotation symmetry around **B**. The FM state has no spontaneously broken symmetries.

2. Kekule (KEK) and fully layer-polarized (FLP) states

For this state,

$$\Delta = \frac{1}{2}\begin{pmatrix} 1+\cos\theta & 0 & \sin\theta & 0 \\ 0 & 1+\cos\theta & 0 & \sin\theta \\ \sin\theta & 0 & 1-\cos\theta & 0 \\ 0 & \sin\theta & 0 & 1-\cos\theta \end{pmatrix}. \tag{34}$$

To specify the angle at the minimum, we need to define an energy g_K:

$$g_K = (3 - r^2)g_z + (2r^2 - 1)|g_{xy}| - (1 - r^2)G_0. \tag{35}$$

In terms of g_K the energy for arbitrary θ can be expressed as

$$\tilde{\mathcal{E}}(\theta) = 8g_0 - 2(1 + r^2)G_0 - 2(1 - r^2)g_z - 2(2r^2 - 1)|g_{xy}| - 4D\cos\theta + 2g_K\cos^2\theta. \tag{36}$$

It is clear that if $g_K < 0$, $\theta = 0$ is the minimum. For $g_K > 0$ we find θ at the minimum to be

$$\cos\theta = \frac{D}{g_K} \quad \forall\ D < g_K; \quad \cos\theta = 1 \quad \forall\ D > g_K. \tag{37}$$

The case $D > g_K$ corresponds to the fully layer-polarized (FLP) state. The energy of the KEK/FLP state is

$$\tilde{\mathcal{E}}_{\rm KEK} = 8g_0 - 2(1 + r^2)G_0 - 2(1 - r^2)g_z - 2(2r^2 - 1)|g_{xy}| - \frac{2D^2}{g_K}, \quad D < g_K \tag{38}$$

$$\tilde{\mathcal{E}}_{\rm FLP} = 8g_0 - 4G_0 + 4g_z - 4D, \quad D > g_K. \tag{39}$$

The KEK/FLP states have no orbital or spin polarization. They do have a valley polarization. The KEK state spontaneously

breaks the valley U(1) symmetry. The FLP state does not spontaneously break any symmetry.

3. *Spin-valley entangled (SVE) state*

This state has the $K\uparrow$ state occupied, but mixes the $K\downarrow$ and $K'\uparrow$ states. In this case,

$$\Delta = \frac{1}{2}\begin{pmatrix} 2 & 0 & 0 & 0 \\ 0 & 1+\cos\psi & \sin\psi & 0 \\ 0 & \sin\psi & 1-\cos\psi & 0 \\ 0 & 0 & 0 & 0 \end{pmatrix}. \tag{40}$$

The energy of this state is evaluated to be

$$\begin{aligned}\tilde{\mathcal{E}}(\psi) &= 4(2g_0 - G_0 - g_z + |g_{xy}| - E_Z) \\ &\quad - 4\cos^2\frac{\psi}{2}(D + 2|g_{xy}| - E_Z - \tilde{D}) \\ &\quad + 4(1-r^2)(g_z - G_0)\cos^4\frac{\psi}{2}. \end{aligned}\tag{41}$$

The optimum value of $\cos^2\frac{\psi}{2}$ is easily found to be

$$\cos^2\frac{\psi}{2} = \frac{D + 2|g_{xy}| - \tilde{D} - E_Z}{2(1-r^2)(g_z - G_0)}. \tag{42}$$

Defining

$$D_{\min}^{\mathrm{SVE}} = \tilde{D} + E_Z - 2|g_{xy}|, \tag{43}$$

$$D_{\max}^{\mathrm{SVE}} = D_{\min}^{\mathrm{SVE}} + 2(1-r^2)(g_z - G_0), \tag{44}$$

the minimum energy of the SVE state for D in the range $D_{\min}^{\mathrm{SVE}} < D < D_{\max}^{\mathrm{SVE}}$ is

$$\tilde{\mathcal{E}}_{\mathrm{SVE}} = 4(2g_0 - G_0 - g_z - E_Z + |g_{xy}|) - \frac{2\left(D - D_{\min}^{\mathrm{SVE}}\right)^2}{\left(D_{\max}^{\mathrm{SVE}} - D_{\min}^{\mathrm{SVE}}\right)}. \tag{45}$$

This state spontaneously breaks a single U(1), which is an entangled combination of valley and spin, and smoothly interpolates between the FLP and the FM states.

Note that as $r^2 \to 1$, Eq. (44) implies that the range of D over which the SVE state exists shrinks to zero. In fact, precisely at $r^2 = 1$ and $D = D_{\min}^{\mathrm{SVE}} = D_{\max}^{\mathrm{SVE}}$ the energy of Eq. (41) becomes independent of ψ. This means that there should be a zero-energy $q = 0$ collective mode at this value of D, which is indeed seen in a recent calculation [29]. This is a hint of the potential existence of the SVE state *even at* $r^2 = 1$.

4. *Broken U(1) × U(1) [BU(1)^2] state*

This is an interesting state that spontaneously breaks the U(1) symmetries of both the spin and valley sectors. We will call this the BU(1)^2 state for short. The most general state for two filled levels, assuming real vectors, can be described by five real parameters. This can be seen as follows: the first filled state is an O(4) vector (real state) which can be specified by three angles. The second filled state also has three angles, but the constraint that it should be orthogonal to the first filled state reduces the total number of independent angles by one, to a total of five.

We have numerically searched in this five-dimensional parameter space for the minimum energy HF state, and found that these minima can always be described by a state requiring only three real angles, which we call θ, χ, ψ. In addition to these there are two U(1) angles upon which the energy does not depend, which we label ϕ and η. Defining $\gamma = \frac{\psi+\chi}{2}$ and $\zeta = \frac{\psi-\chi}{2}$ the resulting Δ matrix may be expressed as

$$\Delta = \frac{1}{2}\begin{pmatrix} 1+\cos\chi\cos\theta & e^{-i\phi}\sin\theta\cos\zeta & e^{i\eta}\sin\theta\sin\zeta & -e^{i(\eta-\phi)}\sin\chi\cos\theta \\ e^{i\phi}\sin\theta\cos\zeta & 1-\cos\psi\cos\theta & -e^{i(\eta+\phi)}\sin\psi\cos\theta & e^{i\eta}\sin\theta\sin\zeta \\ e^{-i\eta}\sin\theta\sin\zeta & -e^{-i(\eta+\phi)}\sin\psi\cos\theta & 1+\cos\psi\cos\theta & -e^{-i\phi}\sin\theta\cos\zeta \\ -e^{-i(\eta-\phi)}\sin\chi\cos\theta & e^{-i\eta}\sin\theta\sin\zeta & -e^{i\phi}\sin\theta\cos\zeta & 1-\cos\chi\cos\theta \end{pmatrix}. \tag{46}$$

The values of ϕ, η will be chosen in the true ground state by spontaneous symmetry breaking. In the limit $\psi = \chi = 0$, this ansatz reduces to the CAF/FM where θ is the canting angle of the CAF/FM. Similarly, for $\chi = 0$, $\psi = \pi$ it reduces to the KEK/FLP state, where θ now means the canting angle of the Kekule state. Thus, Eq. (46) interpolates smoothly between the CAF/FM and the KEK/FLP states; a similar parametrization relating the two states on their coexistence line was presented in Ref. [29]. Finally, $\theta = \chi = \pi$ and $\psi \neq 0,\pi$ correspond to the SVE state. We will reserve the name "broken- U(1) × U(1)" for the state where all three angles θ, χ, ψ are nontrivial, that is, different from 0 or π.

The energy for this ansatz is

$$\begin{aligned}\tilde{\mathcal{E}} &= 8g_0 - 4G_0 - 4g_z - 4\cos\theta(E_Z\cos\gamma\cos\zeta + D\sin\gamma\sin\zeta) + 2\sin^2\zeta(\tilde{D} - 2r^2|g_{xy}|) \\ &\quad + \cos^2\theta(4|g_{xy}| - 4(1-r^2)|g_{xy}|\sin^2\zeta + 2\sin^2\zeta[\tilde{D} - 2|g_{xy}|] + 4\sin^2\gamma\sin^2\zeta(1-r^2)[g_z - G_0]). \end{aligned}\tag{47}$$

Unfortunately, we have not been able to analytically find the minima of $\tilde{\mathcal{E}}$ within its full three-angle domain.

D. Instabilities of CAF/FM, KEK/FLP, and SVE states

Since the three-angle ansatz can describe all the other states that only have a single broken U(1), we can use the three-angle ansatz to find the instabilities of the CAF/FM and the KEK/FLP. Experiments typically scan in both $B_\perp$ and D in order to build up the phase diagram [22–26,35]. In addition, some experiments use the Zeeman coupling (tuned via an in-plane magnetic field) as an additional external parameter

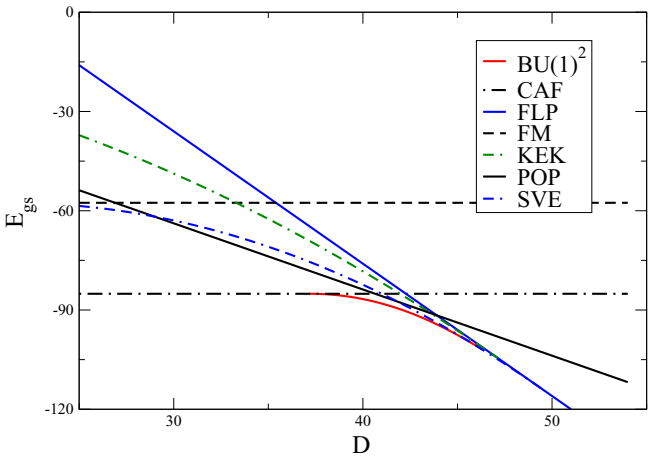

FIG. 2. The energies of the various HF states for a particular choice of parameters. We have fixed $B_\perp = 6$ T, and $E_Z = |g_{xy}|/3$, and plotted the energies as functions of D. The dashed and the dotted-dashed black lines are the FM and CAF energies, respectively. They are independent of D. The solid blue line is the energy of the FLP state (with a slope of -4), while the solid black line is the energy of the POP state (with a slope of -2). The solid red line, where it exists, marks the energy of the BU(1)^2 state. The dottted-double-dashed blue line is the energy of the SVE state, which interpolates smoothly between the FM and FLP states. The dotted-double-dashed green line is the energy of the KEK state. For this particular choice of parameters, as D increases, the system starts in the CAF state for small D, undergoes a second-order transition into the BU(1)^2 state, which then gives way to the SVE state, which in turn yields to the FLP state. All transitions are second order.

to access, for example, the fully spin-polarized phase [26]. Motivated by such experiments, we will analyze the situation where $B_\perp$ and E_Z are fixed while D is varied. We define the critical D at which the CAF/FM becomes unstable to the three-angle ansatz as D_{c1}, while the D at which the KEK/FLP or the SVE/FLP becomes unstable to the three-angle ansatz is defined as D_{c2}. Ignoring the POP state for the moment, a necessary (but not sufficient) condition for the broken U(1) $\times$ U(1) state to exist as a HF state is $D_{c2} > D_{c1}$. By doing this as a function of $B_\perp$, we build up the instability lines in the entire phase diagram.

To make the ideas concrete, Fig. 2 shows the energies of the various HF states as functions of D for fixed $B_\perp = 6$ T, and $E_Z = |g_{xy}|/3$. For this set of parameters, the FM, KEK, and POP states are always higher in energy than the others, and hence are not the ground state at any D. On the other hand, the CAF, the BU(1)^2, the SVE, and the FLP states are the lowest in energy, each in a corresponding range of D. As can be seen, the SVE state interpolates smoothly between the FM and the FLP states. Thus, the FLP and FM states must be linearly unstable to the SVE state at the appropriate values of D. Similarly, the BU(1)^2 state interpolates smoothly between the CAF and SVE states. Thus, the CAF and SVE states must be linearly unstable to the BU(1)^2 state at the appropriate values of D. In the following, we will analytically compute the values of D corresponding to the various linear instabilities.

Let us consider D_{c1} first. Since the CAF/FM state has $\chi = \psi = \gamma = \zeta = 0$, we can consider γ, $\zeta \ll 1$ and expand the energy in powers of γ, ζ. After doing so, we obtain a constant piece (the energy of the CAF/FM state) and a quadratic form in γ and ζ. The instability occurs when the quadratic form has a zero eigenvalue. For the CAF state with $E_Z < 2|g_{xy}|$, after setting $\cos\theta = \frac{E_Z}{2|g_{xy}|}$, we find

$$\tilde{\mathcal{E}} = 4g_0 - 4g_z - 2g_{nz} - \frac{E_Z^2}{|g_{xy}|} + M_{\zeta\zeta}\zeta^2 + M_{\gamma\gamma}\gamma^2 - \frac{2DE_Z}{|g_{xy}|}\gamma\zeta, \tag{48}$$

$$M_{\gamma\gamma} = \frac{E_Z^2}{2g_{xy}^2}[|g_{xy}| + (1-r^2)G_0 + (1+r^2)g_z], \tag{49}$$

$$M_{\zeta\zeta} = \frac{r^2E_Z^2}{|g_{xy}|} + 2[(1-r^2)G_0 + (1+r^2)g_z - (2r^2-1)|g_{xy}|]. \tag{50}$$

Recalling the definition of $\tilde{D}$ [Eq. (30)] we can express Eqs. (49) and (50) as

$$M_{\gamma\gamma} = \tilde{D}\frac{E_Z^2}{2|g_{xy}|^2}, \tag{51}$$

$$M_{\zeta\zeta} = 2(\tilde{D} - 2r^2|g_{xy}|) + \frac{r^2E_Z^2}{|g_{xy}|}. \tag{52}$$

The critical value D_{c1} for the CAF case is then

$$D_{c1}^{\mathrm{CAF}} = \frac{|g_{xy}|}{E_Z}\sqrt{M_{\gamma\gamma}M_{\zeta\zeta}} \tag{53}$$

$$= \sqrt{\tilde{D}\left(\tilde{D} - 2r^2|g_{xy}| + \frac{r^2E_Z^2}{2|g_{xy}|}\right)}. \tag{54}$$

For the FM state ($E_Z > 2|g_{xy}|$), setting $\theta = 0$ we obtain

$$\tilde{\mathcal{E}} = 4g_0 - 4g_z - 2g_{nz} - 4E_Z + 4|g_{xy}| - 4D\gamma\zeta + M_{\zeta\zeta}\zeta^2 + M_{\gamma\gamma}\gamma^2, \tag{55}$$

$$M_{\zeta\zeta} = M_{\gamma\gamma} = 2(2\tilde{D} + E_Z - 2|g_{xy}|). \tag{56}$$

In this case, the critical value is

$$D_{c1}^{\mathrm{FM}} = \tilde{D} + E_Z - 2|g_{xy}|. \tag{57}$$

Now, let us turn to D_{c2}, the critical value of D where the KEK/FLP or the SVE/FLP state is unstable to the three-angle ansatz. We start from large D where the FLP state is clearly the HF ground state. In this case, since $\theta \approx 0$, $\chi \approx 0$, $\psi \approx \pi$ we can assume $\theta \ll 1$, $\gamma = \frac{\pi}{2} - \xi$, $\zeta = \frac{\pi}{2} - \omega$, and expand the energy function for small θ, ξ, ω. Due to the fact that the energy function (47) depends on θ only via $\cos\theta$, we see that the quadratic fluctuations of θ decouple from those of γ, ζ. The quadratic instability of the FLP state in the θ channel occurs at

$$D_c^\theta = D_c^{\mathrm{FLP/KEK}} = g_K \tag{58}$$

and leads to the KEK state which we have already described.

Ignoring the θ flucuations, the energy function near the FLP state can be expanded for small ξ, ω as

$$\tilde{\mathcal{E}} = \tilde{\mathcal{E}}_{\mathrm{FLP}} + 2(D - 4g_z + \tilde{D})(\xi^2 + \omega^2) - 4E_Z\xi\omega. \tag{59}$$

This leads to

$$D_{c,\mathrm{FLP}}^{\xi,\omega} = D_c^{\mathrm{FLP/SVE}} = 4g_z - \tilde{D} + E_Z. \tag{60}$$

This instability leads to the SVE state which we have also described. Using Eqs. (30) and (35), we note that

$$D_c^{\mathrm{FLP/SVE}} = D_c^{\mathrm{FLP/KEK}} - 2r^2|g_{xy}| + E_Z \tag{61}$$

implying that the SVE (KEK) is favored for $E_Z > 2r^2|g_{xy}|$ ($E_Z < 2r^2|g_{xy}|$). In either case, the linear instability of the FLP state leads to a state with a *single* broken U(1). Thus, in order to see where the BU(1)^2 state terminates as D increases from D_{c_1}, we need to consider the linear instabilities of the KEK and SVE states.

First consider the KEK state, which is stable when $D < g_K$. Once again, the θ fluctuations decouple from those of the other two angles. The energy function to quadratic order in ξ, ω is

$$\tilde{\mathcal{E}} = \frac{\mathcal{E}_{\mathrm{KEK}}}{N_\phi} + \frac{4r^2D^2|g_{xy}|}{g_K^2}\xi^2 - \frac{4DE_Z}{g_K}\xi\omega + M_{\omega\omega}\omega^2,$$

$$M_{\omega\omega} = 4r^2|g_{xy}| - 2\left(1 - \frac{D^2}{g_K^2}\right)\tilde{D}. \tag{62}$$

We infer the value of D_{c2} from this equation to be

$$D_{c2}^{\mathrm{KEK}} = g_K\sqrt{1 - \frac{2r^2|g_{xy}|}{\tilde{D}} + \frac{E_Z^2}{2r^2\tilde{D}|g_{xy}|}}. \tag{63}$$

In order for the KEK state to be stable, we must impose $D_{c2} < g_K$, consistent with the requirement $E_Z < 2r^2|g_{xy}|$. We thus identify a first parameter regime in which BU(1)^2 state is the ground state for a nonvanishing range of D.

For $E_Z > 2r^2|g_{xy}|$ the KEK state has no linear instabilities. If its energy crosses that of the CAF/FM state it must do so as a first-order transition.

Now, we turn to the linear instabilities of the SVE state. The SVE state corresponds to $\theta = \xi = \pi$ while ψ is nontrivial. The θ fluctuations once again decouple from the ξ, ψ fluctuations. The ξ, ψ fluctuations are innocuous, but the θ fluctuations do lead to an instability. A straightforward analysis shows that

$$D_{c2}^{\mathrm{SVE}} = D_{\mathrm{min}}^{\mathrm{SVE}} + \frac{2|g_{xy}| - E_Z}{|g_{xy}|}(g_z - G_0). \tag{64}$$

Recalling the condition for the existence of the SVE state to be $D_{\mathrm{min}}^{\mathrm{SVE}} < D < D_{\mathrm{min}}^{\mathrm{SVE}} + 2(1 - r^2)(g_z - G_0)$, we indeed see that this is an actual instability only for $E_Z > 2r^2|g_{xy}|$. We then arrive at a second scenario in which the BU(1)^2 state is stable, in this case connecting either the CAF state at $D = D_{c_1}^{\mathrm{CAF}}$ (for $E_z < 2|g_{xy}|$) or the FM state at $D = D_{c_1}^{\mathrm{FM}}$ (for $E_z > 2|g_{xy}|$) to the SVE state at $D = D_{c_2}^{\mathrm{SVE}}$.

Finally, if $E_Z < 2r^2|g_{xy}|$ and the energy of the SVE state crosses that of the CAF/FM, it must do so as a first-order transition.

V. MAIN RESULTS AND PHASE DIAGRAMS

As seen in the previous section, there are several different states that compete in different regimes of $B_\perp$, E_Z, D. We will assume that all the couplings g_i are proportional to $B_\perp$. It would then naively appear that one can scale out $B_\perp$ from the Hamiltonian. However, recall that the parameters r and ϵ_a depend on $B_\perp$ via their dependence on λ [see Eq. (4)] arising from the trigonal warping coefficient t_3.

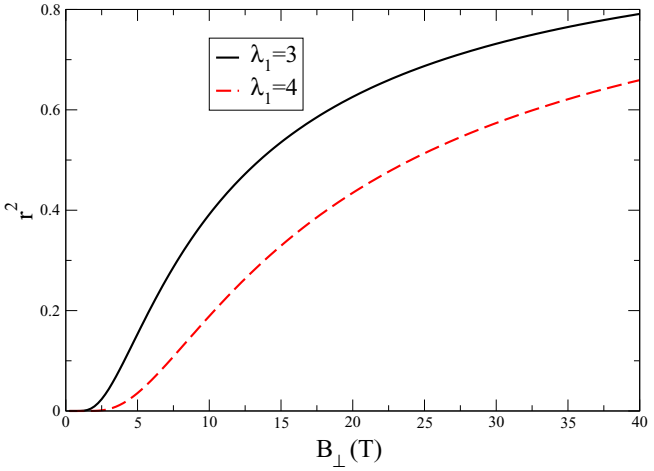

FIG. 3. r^2 vs $B_\perp$ for $\lambda_1 = 3$ and 4. Note that r^2 tends vary rapidly to zero when $B_\perp$ falls below a characteristic scale set by λ_1. At large values of $B_\perp$, $r^2 \to 1$. The approach to $r^2 = 1$ is very slow.

Introducing a field-independent parameter $\lambda_1 = \lambda\sqrt{B_\perp}$ (which is the value of λ at $B_\perp = 1$ T), in Figs. 3 and 4 we show r^2 vs $B_\perp$ and ϵ_a vs $B_\perp$ for $\lambda_1 = 3$ and 4. We see that both r^2 and ϵ_a vanish very rapidly for $B_\perp$ smaller than a characteristic scale B_λ. For $B_\perp \gg B_\lambda$, we see that $r^2 \to 1$ while ϵ_a becomes linear in $B_\perp$. There are thus two regimes in which the analysis becomes simple. In the small-$B_\perp$ regime, we can essentially set $r^2 \approx 0$. In the large-$B_\perp$ regime, we can set $r^2 \approx 1$. With the parameters we use, the small-$B_\perp$ regime is far easier to realize at experimentally feasible values of $B_\perp$.

Before presenting the numerical HF results we analyze the phase diagram for small and large $B_\perp$ analytically. This provides us with relations between the couplings g_i that determine the topology of the phase diagram.

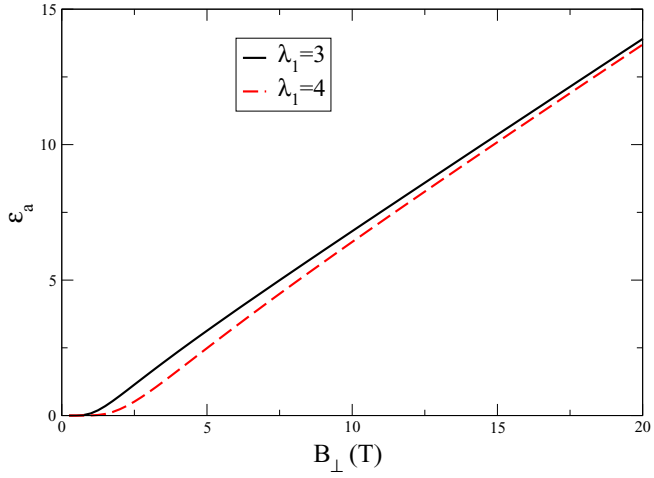

FIG. 4. Orbital anisotropy energy ϵ_a vs $B_\perp$ for $\lambda_1 = 3$ and 4. At very small values of $B_\perp$ below a characteristic scale set by λ_1, ϵ_a vanishes rapidly as $B_\perp \to 0$. At large values of $B_\perp$, ϵ_a becomes linear in $B_\perp$.

A. Possible phase diagrams at small $B_\perp$

The key idea is to analyze the ordering of the various special values of D that we defined in Sec. IV D in the limit $r^2 \to 0$. They are

$$\tilde{D} \approx g_z + G_0 + |g_{xy}|, \tag{65}$$

$$g_K \approx 3g_z - G_0 - |g_{xy}| \approx 4g_z - \tilde{D}, \tag{66}$$

$$D_{c1}^{\mathrm{CAF}} \approx \tilde{D}, \tag{67}$$

$$D_{c1}^{\mathrm{FM}} = \tilde{D} + E_Z - 2|g_{xy}|, \tag{68}$$

$$D_{c2}^{\mathrm{SVE}} = \tilde{D} + E_Z - 2|g_{xy}| + \tfrac{2|g_{xy}| - E_Z}{|g_{xy}|}(g_z - G_0). \tag{69}$$

We have not included D_{c2}^{KEK} because the condition for it to exist, $E_Z < 2r^2|g_{xy}|$, cannot be satisfied when $r^2 \to 0$. The condition for the BU(1)^2 state to be the true HF ground state is $D_{c2} > D_{c1}$. For $E_Z < 2|g_{xy}|$, this becomes

$$g_z > G_0 + |g_{xy}|. \tag{70}$$

If $E_Z > 2|g_{xy}|$, then D_{c2}^{SVE} ceases to be physical (because it becomes less than $D_{\mathrm{min}}^{\mathrm{SVE}}$). In this case there is no BU(1)^2 state. Instead, as D increases, the FM state gives way to the SVE state at D_{c1}^{FM}, which in turn continuously evolves to become the FLP state at $D_c^{\mathrm{FLP/SVE}} = 4g_z - \tilde{D} + E_Z$, as long as

$$g_z > G_0. \tag{71}$$

Thus, we obtain the following three possibilities at small $B_\perp$: (i) If $g_z < G_0$, there will be a direct first-order transition of the CAF/FM into either of the SVE/FLP states at all values of E_Z. (ii) If $G_0 < g_z < G_0 + |g_{xy}|$, then there will be a direct first-order transition between the CAF and FLP/SVE states as D increases as long as $E_Z < 2|g_{xy}|$. However, for $E_Z > 2|g_{xy}|$, the SVE state smoothly interpolates between the FM at small D to the FLP state at large D. All transitions will now be continuous. (iii) If $g_z > G_0 + |g_{xy}|$, then the BU(1)^2 state always intervenes between the CAF and the SVE states as D is increased for $E_Z < 2|g_{xy}|$. However, for $E_Z > 2|g_{xy}|$, the BU(1)^2 state disappears, and instead the SVE smoothly connects the FM and FLP states.

Now, we consider the POP state, and the criteria for whether it is the true ground state for the small-$B_\perp$ regime in which $r^2 \to 0$. Some insight can be obtained as follows. Consider the interlayer potential $D \equiv D_{\mathrm{FLP}}^*$ at which the CAF and FLP states are equal in energy [Eqs. (32) and (39)]. Recall that the slope of the POP state with respect to D is -2, while that of the FLP state is -4. We evaluate the energy of the POP state at $D = D_{\mathrm{FLP}}^*$. If $\tilde{\mathcal{E}}_{\mathrm{POP}}(D_{\mathrm{FLP}}^*) > \tilde{\mathcal{E}}_{\mathrm{CAF}}$, then the POP state will not be the ground state for any D. For purely perpendicular field, assuming $E_Z \ll 2|g_{xy}|$, we have $D_{\mathrm{FLP}}^* \approx 2g_z$. Since for $r^2 \to 0$ we have $\epsilon_a \approx 0$, this leads to the condition for the absence of the POP state,

$$G_0 + |g_{xy}| - g_z + \tfrac{3}{2}g_{nz} > 0. \tag{72}$$

Recall that in order to see the BU(1)^2 state at minimal E_Z, and assuming $E_Z \ll 4|g_{xy}|$, we need $g_z > G_0 + |g_{xy}|$. This means in order for the BU(1)^2 state to be the lowest in energy among the orbitally symmetric states, and for it to have a lower energy than the POP state, we need g_{nz} greater than some critical value. This is easily understood, as a large, positive g_{nz} penalizes orbital polarization.

Let us now turn to the other extreme: very large values of $B_\perp$ such that $r^2 \to 1$ and $\epsilon_a = \epsilon_{a0}B_\perp$.

B. Possible phase diagrams at large $B_\perp$

Setting $r^2 \approx 1$ we find

$$\tilde{D} \approx 2g_z + |g_{xy}|, \tag{73}$$

$$g_K \approx 2g_z + |g_{xy}| = \tilde{D}, \tag{74}$$

$$D_{c1}^{\mathrm{CAF}} \approx \sqrt{\tilde{D}\Big(\tilde{D} - 2|g_{xy}| + \tfrac{E_Z^2}{2|g_{xy}|}\Big)}, \tag{75}$$

$$D_{c1}^{\mathrm{FM}} = \tilde{D} + E_Z - 2|g_{xy}| = 2g_z - |g_{xy}| + E_Z, \tag{76}$$

$$D_{c2}^{\mathrm{KEK}} \approx \sqrt{\tilde{D}\Big(\tilde{D} - 2|g_{xy}| + \tfrac{E_Z^2}{2|g_{xy}|}\Big)}. \tag{77}$$

For $E_Z < 2|g_{xy}|$ we see that $D_c^{\mathrm{FLP/KEK}} = g_K > D_c^{\mathrm{FLP/SVE}}$, which means that one should consider D_{c1}^{CAF} and D_{C2}^{KEK}. However, in the $r^2 \to 1$ limit, these are identical! This means the window for the BU(1)^2 state shrinks to zero as $r^2 \to 1$. The same is true for $E_Z > 2|g_{xy}|$.

At $r^2 = 1$ and $D = D_{c1}^{\mathrm{CAF}} = D_{c2}^{\mathrm{KEK}}$ the energy becomes independent of two of the three angles. This implies a $q = 0$ collective mode whose energy vanishes, as has been found in a recent calculation [29]. Thus, hints of the potential existence of the BU(1)^2 state can be seen in the collective mode spectrum even at $r^2 = 1$.

We see then that the trigonal warping t_3, via the parameter $r^2 < 1$, is responsible for the existence of the BU(1)^2 phase in a nonvanishing region of the parameter space. For this reason previous theoretical analyses, which in general have not included the effects of t_3, have not identified this state in the phase diagram.

C. Hartree-Fock phase diagrams

Since the space of couplings is so large, we will take some guidance from experiments to narrow our choices. The POP state has been seen in experiments on BLG at $\nu = 0$: at purely perpendicular fields, it makes its appearance for $B_\perp > 12$ T [25]. In some experiments, a direct transition [25] is seen between a putative CAF state at small D and a putative FLP state at larger D, while in others there are intriguing hints that there may be an intermediate phase between the CAF and the FLP at small $B_\perp$ [24,26]. Presumably, disorder, the screening environment, or perhaps microscopic features of how the samples are prepared, determine whether the intermediate phase is seen. A second result we will take from experiments is that when one tries to fit the observed sequence of transitions to a single-particle model, the anisotropy energy appears to be close to zero for $B_\perp < 10$ T but turns on afterwards [35]. Looking at Fig. 4 we see that there is a similar behavior of ϵ_a vs $B_\perp$. This allows us to conjecture that the effective value of λ is rather larger than conventionally assumed.

To account for this diversity of observations, we will consider three sets of parameters embodying the three regimes

of g_z that we obtained in Sec. V A for small $B_\perp$. Parameter set 1 (PS1) will have $g_z > G_0 + |g_{xy}|$, so that there is an intervening broken U(1) × U(1) phase as a function of D between the CAF and the FLP phases for $E_Z < 2|g_{xy}|$. Parameter set 2 (PS2) will have $G_0 < g_z < G_0 + |g_{xy}|$. This means that at the minimal E_Z there is a direct first-order transition between the CAF and SVE phases, while for $E_Z > 2|g_{xy}|$ the SVE phase smoothly connects the FM state to the FLP state. Parameter set 3 (PS3) will have $G_0 > g_z$, so that there is always a direct first-order transition between the CAF and FLP phases.

1. Parameter set 1

The values we use (arbitrary units) are $g_0 = 0.5B_\perp$, $g_z = 3.5B_\perp$, $g_{xy} = -1.65B_\perp$, and $g_{nz} = 1.0B_\perp$. The dimensionless parameter λ of Eq. (4) is assumed to be $\lambda = 5.0/\sqrt{B_\perp}$. In order to keep the POP state from appearing below about 12 T, we set the orbital anisotropy to $\tilde{\epsilon}_a = 1.4$. Since we are using arbitrary units for the couplings g_i, our results for the values of D at which transitions take place are also arbitrary. Therefore, in the phase diagrams that follow, we will not put units on the D axis.

Let us first consider the case of a perpendicular field only. From experimental measurements [26], the total field needed to spin polarize a sample at $B_\perp = 2$ T is about 12 T. We combine this with the theoretical critical Zeeman coupling for full spin polarization, $E_Z = 2|g_{xy}|$, to obtain $E_Z = \frac{1}{3}|g_{xy}|$ for a purely perpendicular field. The phase diagram for this situation is shown in Fig. 5. As can be seen, most of the phases discussed before appear in the phase diagram. Let us first focus on the small-$B_\perp$ region, where we expect $r^2 \ll 1$. In accordance with the expectations of Sec. V A, we see that with increasing D, one encounters, in order, the CAF, BU(1)^2, SVE, and FLP states, all of which are identified from the numerically generated Δ matrix. Figure 6 illustrates the spin polarization S_z and the valley polarization τ_z at fixed $B_\perp = 6$ T as a function of D. At this field, the CAF gives way to the BU(1)^2 state at around $D = 36$. At $D \approx 46$ a slight kink in the lines indicates that the system has made a transition to the SVE state. The SVE state is stable in the interval $46 \leq D \leq 50$, and for $D > 50$ the system is in the FLP state.

At larger $B_\perp > 11$ T, the POP state makes its appearance by "eating up" some of the regime that belongs to the BU(1)^2 state. An illustrative cut at $B_\perp = 16$ T is shown in Fig. 7, which in addition to S_z and τ_z illustrates O_z, the orbital polarization. Now we see that the system undergoes a second-order transition from the CAF state to the BU(1)^2 state at $D \approx 102$. This is followed by a first-order transition to the POP state at $D \approx 107$, which then persists until $D \approx 118$. The system now undergoes a first-order transition to a narrow sliver of the BU(1)^2 state, which gives way to the KEK state at $D \approx 122$. The KEK state persists until $D \approx 130$ beyond which the system is in the FLP state.

For completeness, we present two other phase diagrams. In Fig. 8, we consider an intermediate value of tilted field with $E_Z = |g_{xy}|$. The low-D phase is still the CAF state. Note that the SVE phase expands its domain compared to Fig. 5, and the BU(1)^2 state has a correspondingly smaller domain. The KEK state has disappeared altogether. This is because, unlike the SVE state, it has no spin polarization and thus cannot take advantage of the Zeeman field. The domain of the POP state has also expanded, and now it reaches down to $B_\perp = 8$ T.

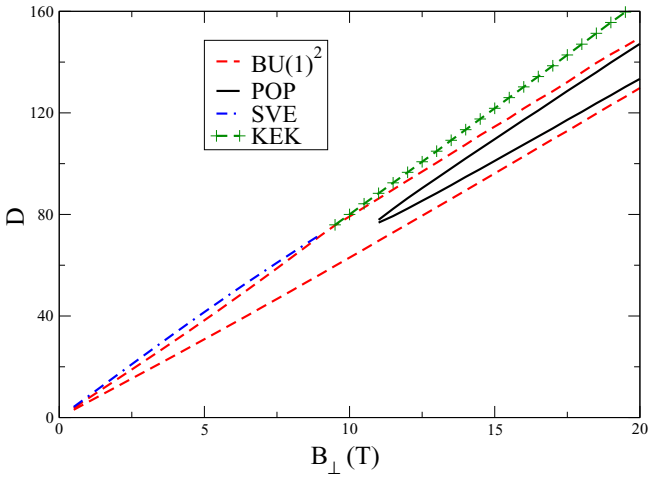

FIG. 5. The $B_\perp$-D phase diagram for PS1 for the case of only perpendicular field. Here and in the following, D is in arbitrary units. This is identical to Fig. 1, reproduced here for convenience. At small D, the system is always in the CAF phase. For $B_\perp < 11$ T, as D increases, the system undergoes a second-order phase transition (dashed red line) to the BU(1)^2 phase. Another second-order phase transition (dashed red line) takes the system at a slightly higher D to the SVE state. Finally, at an even higher D (dashed-dotted blue line) the system goes into the FLP phase. For $B_\perp > 11$ T the POP state becomes lower in energy than the BU(1)^2 state for an intermediate range of D, and is the ground state between the two solid black lines. At higher $B_\perp$, the BU(1)^2 state gives way to the KEK state at the dashed red line, which in turn gives way to the FLP state at the green dashed line with the + symbols.

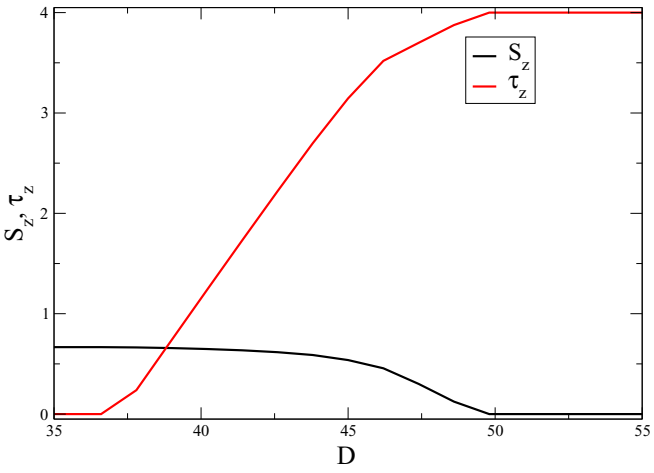

FIG. 6. Order parameters at $B_\perp = 6$ T for PS1 with purely perpendicular field. Recall that D is in arbitrary units. For $D < 36$, the system is in the CAF phase. It makes a second-order transition to the BU(1)^2 phase at $D = 36$ and remains in this phase until $D = 46$, at which point it makes another second-order transition into the SVE phase. The SVE phase persists until about $D = 50$, beyond which the system is fully layer polarized.

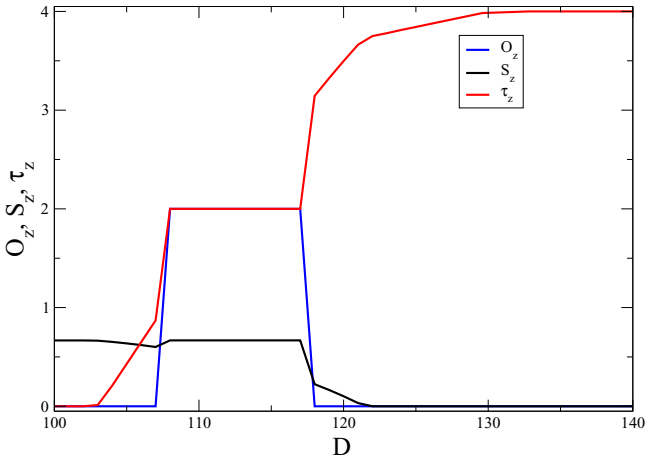

FIG. 7. Order parameters at $B_\perp = 16$ T for PS1 with purely perpendicular field. Once again, the system is in the CAF state for small D. At around $D = 102$, there is a second-order transition into the BU(1)^2 state. This is followed by a first-order transition into the POP state at $D = 107$. The POP state persists until $D = 118$, at which point the system makes a first-order transition back into the BU(1)^2 state. At about $D = 122$ there is another second-order transition, this time into the KEK state. Finally, at about $D = 130$, the KEK state gives way to the FLP state.

In Fig. 9, we present the phase diagram for a very large tilted field of $E_Z = 2.5|g_{xy}|$. The low-D phase is now the FM state. We see that the BU(1)^2 state has disappeared. The SVE and POP states are better able to take advantage of the large E_Z at intermediate values of D.

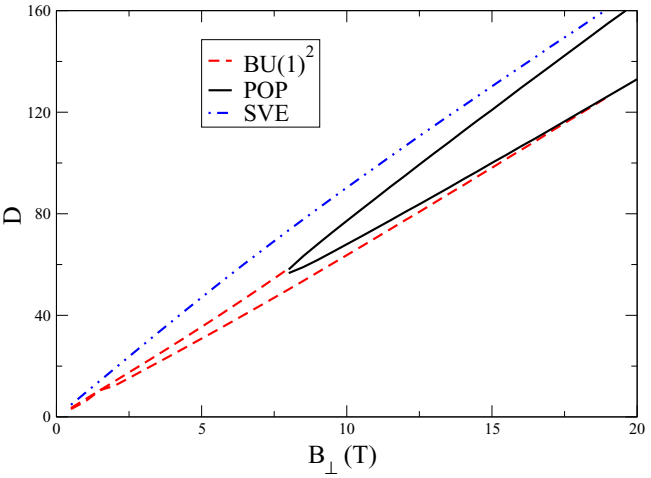

FIG. 8. Phase diagram for PS1 in a tilted field, such that $E_Z = |g_{xy}|$. The BU(1)^2 state appears between the dashed red lines, while the POP state appears between the solid black lines. The main qualitative difference between this figure and Fig. 5 is the absence of the KEK state at large $B_\perp$, where it has been supplanted by the SVE state. All transitions are second order except for those into and out of the POP state.

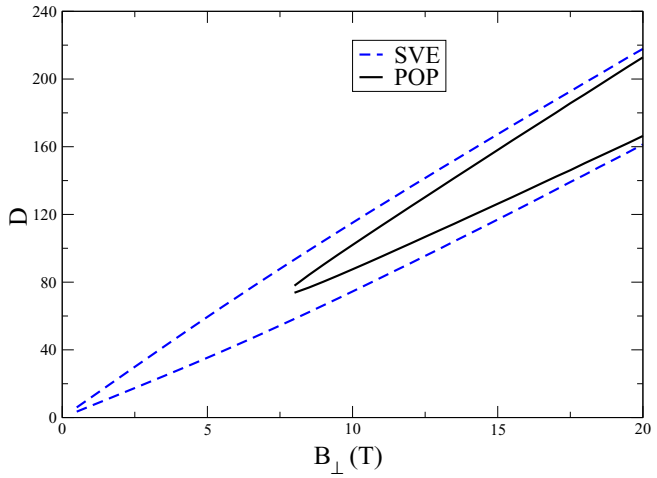

FIG. 9. Phase diagram for PS1 at $E_Z = 2.5|g_{xy}|$. The small-D region is now in the fully spin-polarized FM state, which makes a second-order transition (lower dashed blue line) to the SVE state, which in turn gives way to the FLP state via another second-order transition (upper dashed blue line). The BU(1)^2 state has disappeared and has been supplanted by the SVE state. The POP state intrudes into the SVE region via first-order transitions (solid black lines).

2. Parameter set 2

This set of parameters is identical to PS1, except $g_z = 2.5B_\perp$. This change means that now $G_0 < g_z < G_0 + |g_{xy}|$. Furthermore, to keep the POP state from appearing below $\simeq$10 T, we need to increase the dimensionless orbital anisotropy to $\tilde{\epsilon}_a = 1.77$. Figure 10 shows the phase diagram for PS2 with a purely perpendicular field ($E_Z = |g_{xy}|/3$). As can be seen, the BU(1)^2 phase has almost disappeared from the phase diagram. There is a tiny remnant of it for 8 T $< B_\perp <$ 10 T.

There are several differences in the phase diagrams between PS1 and PS2. Focusing first on small $B_\perp$, the CAF goes into the SVE phase via a first-order transition, without going through the BU(1)^2 phase. The SVE phase gives way to the FLP phase at larger D via a second-order transition. Figure 11 shows the evolution of the order parameters with D for fixed $B_\perp = 2$ T. In Fig. 12 we show the evolution of the order parameters at $B_\perp = 10$ T, which includes a sliver of the BU(1)^2 state. The evolution of the order parameters at $B_\perp = 16$ T is presented in Fig. 13.

For completeness, we examine PS2 for larger Zeeman values. In Fig. 14 we present the phase diagram for PS2 at $E_Z = |g_{xy}|$. For $B_\perp < 8$ T, there are only two transitions as D increases. First, the CAF goes into the SVE state via a first-order phase transition, and then the SVE state gives way to the FLP state via a second-order transition. For larger $B_\perp >$ 8 T, the CAF goes directly into the POP state via a first-order transition. The system then makes another first-order transition into the SVE state, which finally undergoes a second-order transition into the FLP state. Note also that the POP state, being able to take advantage of the larger Zeeman coupling, now appears at smaller values of $B_\perp$ as compared to the case of perpendicular field only.

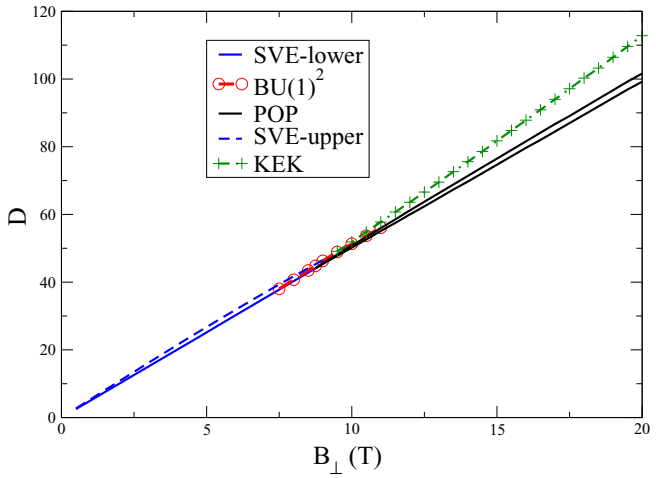

FIG. 10. Phase diagram for PS2 at $E_Z = |g_{xy}|/3$ (purely perpendicular field.) The small-D region is in the CAF phase. For small $B_\perp < 8$ T the CAF makes a direct first-order transition into the SVE phase (solid blue line), which then gives way to the FLP phase via a second-order transition (dashed blue line). Between 8 and 10 T, the situation is very complicated at intermediate D, where many phases are almost identical in energy. At 10 T, as one increases D, there is a direct first-order transition from the CAF phase into the POP state (lower solid black line). The system exits the POP state via another first-order transition into a narrow sliver of the BU(1)^2 state, which exists between the upper solid black line and the red line with circles. The BU(1)^2 state enters the KEK state via a second-order phase transition. Finally, the KEK state gives way to the FLP state. At larger $B_\perp$, the situation simplifies: The CAF makes a first-order transition into the POP, which makes another first-order transition into the KEK, which finally makes a second-order transition to the FLP state (dashed green line with + symbols).

In Fig. 15 we present the phase diagram for PS2 at large Zeeman coupling $E_Z = 2.5|g_{xy}|$. The low-D phase is now the FM state. This implies that the transition from the FM to the

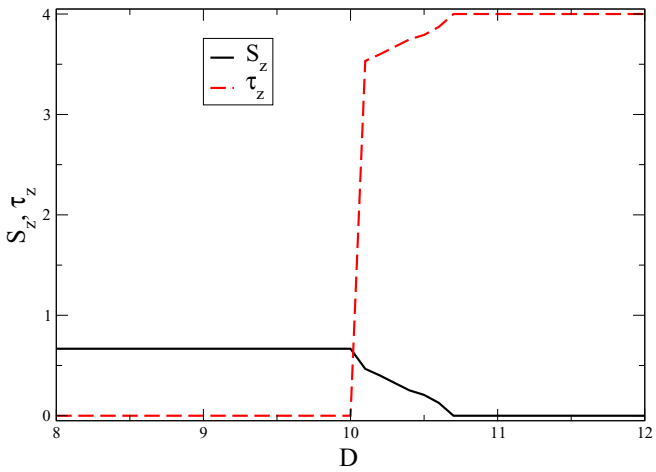

FIG. 11. Order parameters as a function of D at $B_\perp = 2$T in PS2 for purely perpendicular field. The first-order nature of the transition between the CAF and the SVE states is clear. The SVE order parameters smoothly go over to those of the FLP.

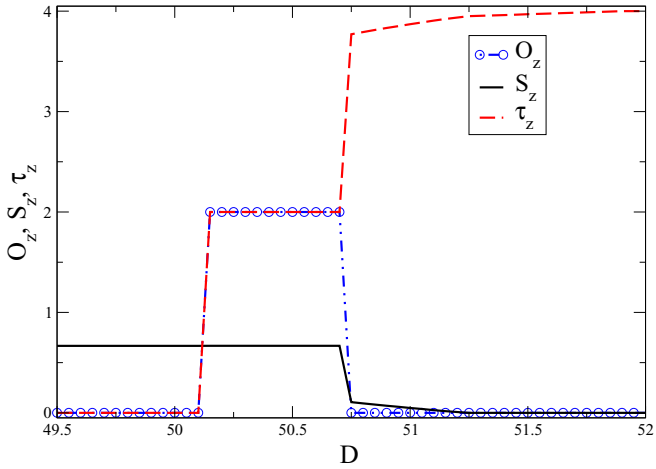

FIG. 12. Order parameters as a function of D at $B_\perp = 10$ T in PS2 for purely perpendicular field. At small D, the system is in the CAF phase. It makes a first-order transition into the POP state at $D = 50.1$. The POP state gives way to the BU(1)^2 state via a first-order transition at $D = 50.75$. The BU(1)^2 state persists until $D = 51.25$, at which point the system makes a second-order transition to the KEK state. Finally, at $D = 52$, the KEK state gives way to the FLP state via a second-order transition.

SVE state should be second order since the SVE smoothly interpolates between the FM and the FLP. Indeed, in Fig. 16, a cut at $B_\perp = 2$ T showing the evolution of the order parameters as a function of D exhibits the second-order nature. At larger values of $B_\perp$, the POP state intervenes and two additional first-order phase transitions, into and out of the POP state, appear, as seen in Fig. 17.

3. *Parameter set 3*

For PS3, we need to have $g_z < G_0$. So, we choose the following values: $g_0 = 1.5B_\perp$, $g_z = 1.75B_\perp$, $g_{xy} =$

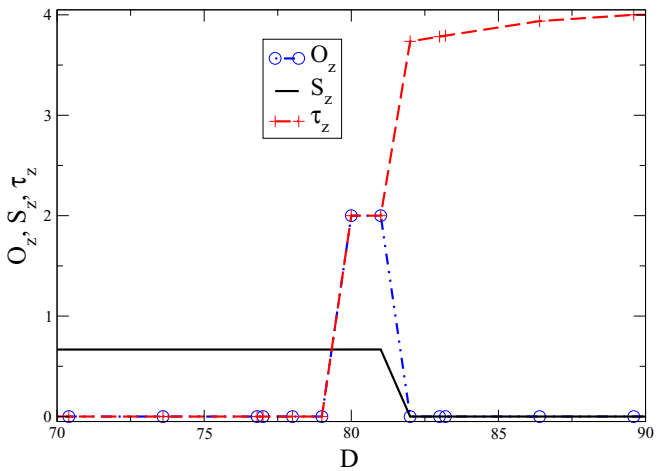

FIG. 13. Order parameters as a function of D at $B_\perp = 16$ T in PS2 for purely perpendicular field. As D increases, the first two transitions, from the CAF into the POP, and from the POP into the KEK state, are first order. The final transition from the KEK to the FLP state is second order.

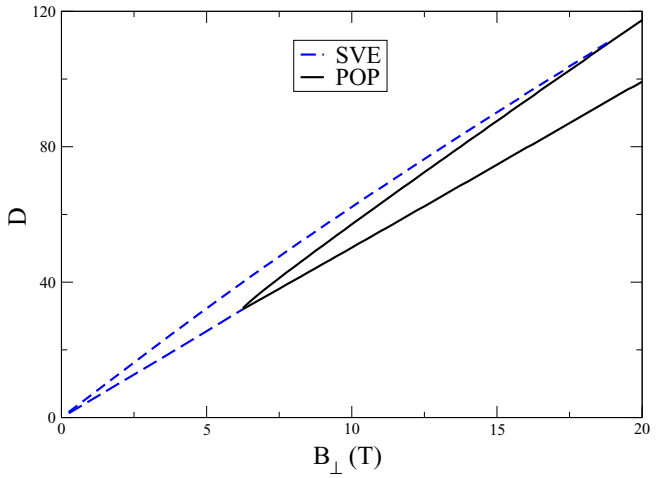

FIG. 14. Phase diagram for PS2 in a tilted field, such that $E_Z = |g_{xy}|$. Only the CAF, the SVE, FLP, and the POP appear. The transitions between the CAF, SVE, and FLP states (dashed blue lines) are second order, while those from the POP state (solid black lines) are first order.

$-1.65B_\perp$, $g_{nz} = B_\perp$, and keep $\lambda_1 = 5$. In order to have the POP state not appear below $B_\perp = 12$ T at purely perpendicular field, we have to increase the value of the dimensionless orbital anisotropy to $\tilde{\epsilon}_a = 3.8$.

In Fig. 18 we show the phase diagram for PS3 at purely perpendicular field. This is the simplest topology of the phase diagram, and only the CAF, FLP, and POP states appear. All the transitions are first order.

In Fig. 19 we show the phase diagram at an intermediate value of the Zeeman coupling $E_Z = |g_{xy}|$. Apart from the POP state appearing at lower $B_\perp$, and extending to larger D, there are no qualitative differences from the case of purely perpendicular field.

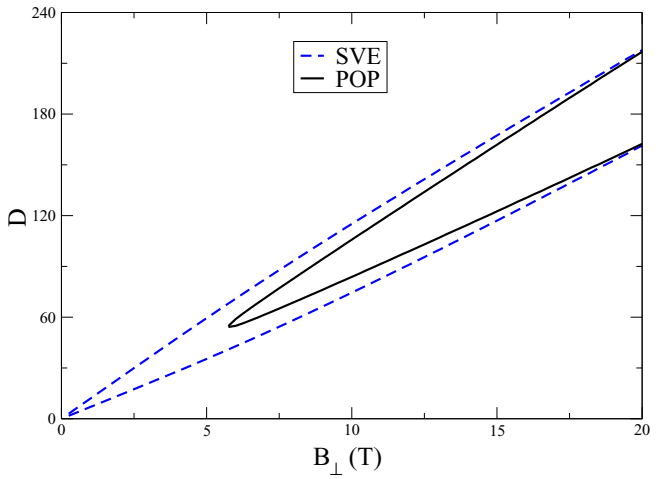

FIG. 15. The phase diagram for PS2 in a large Zeeman field $E_Z = 2.5|g_{xy}|$. Only the FM phase (at small D), the SVE, the FLP (at large D), and the POP phases appear.

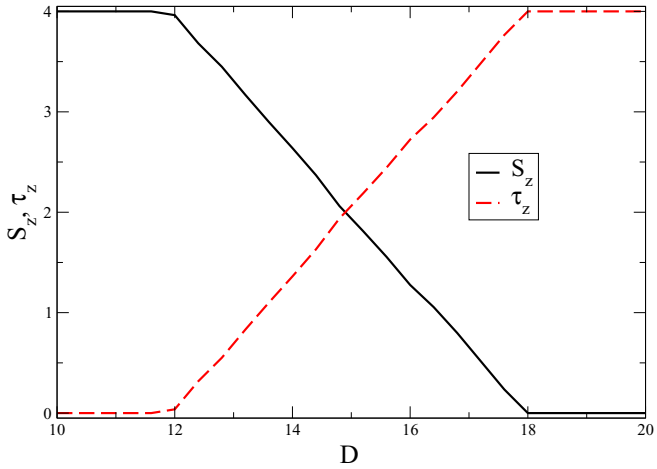

FIG. 16. Order parameters for $B_\perp = 2$ T in PS2 at large Zeeman coupling, such that $E_Z = 2.5|g_{xy}|$. The small-D phase is the fully spin-polarized FM. This makes a second-order phase transition into the SVE, which smoothly interpolates to the FLP state via another second-order phase transition.

VI. DISCUSSION

A. Experimental signatures of the phase transitions

We begin this section by discussing possible experimental signatures of the phases and transitions discussed above.

To our knowledge, three types of measurements have been performed on BLG in the quantum Hall regime: transport, compressibility, and layer polarizability. With respect to transport, all the bulk states we have analyzed are insulators with a charge gap. Deep within a phase, transport occurs only at the edges. In BLG, all quantum numbers except spin are broken by the edge potential; because of this, the FM state is expected to be a quantum spin Hall state [36–39] whereas the others

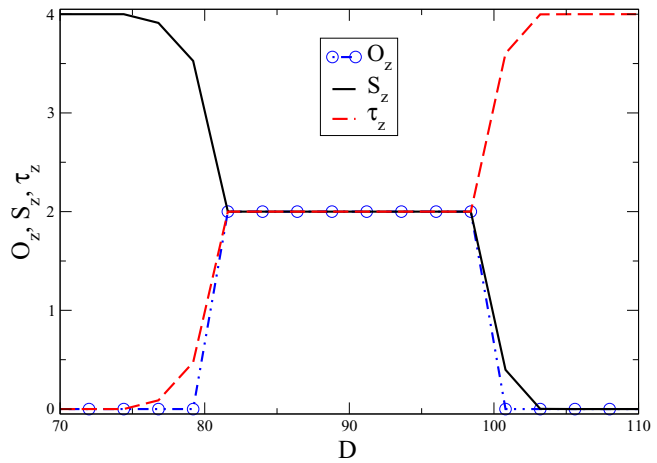

FIG. 17. Order parameters at $B_\perp = 12$ T in PS2 at a large Zeeman coupling $E_Z = 2.5|g_{xy}|$. The small-D phase is the fully spin-polarized FM. This makes a second-order phase transition into the SVE. The POP state intrudes via a first-order transition into the SVE. Another first-order transition takes the system back into the SVE, which smoothly interpolates to the FLP state via another second-order phase transition.

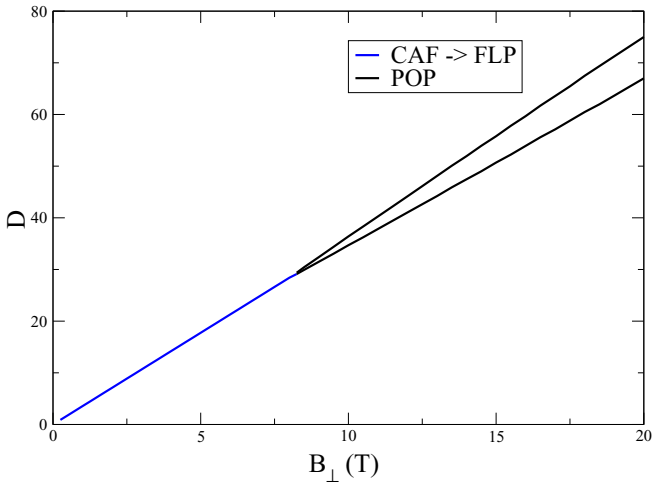

FIG. 18. Phase diagram for PS3 at purely perpendicular field $E_Z = |g_{xy}|/3$. All the transitions are first order. The CAF gives way directly to the FLP at small $B_\perp$, whereas the POP state intrudes for larger $B_\perp$.

are trivial nonconducting states [32,33,40,41]. A transition between two bulk phases is typically seen experimentally either as a peak in the two-terminal conductance [22–24,26,35] or as peaks in the compressibility and/or layer polarizability [25].

Focusing first on the two-terminal conductance, it can have a peak at the transition due to two distinct mechanisms. First, if the transition is second order and has at least one broken U(1) symmetry on at least one side of the transition (all our second-order transitions have this property), we may expect the stiffness of the broken U(1) angle to vanish at the transition. This leads to gapless charged *edge* excitations, as the present authors have established in monolayer graphene [32,33]. Second, if the transition is first order, one may expect the formation of domains due to disorder. Presumably charged excitations are attracted to the domain walls, and if they

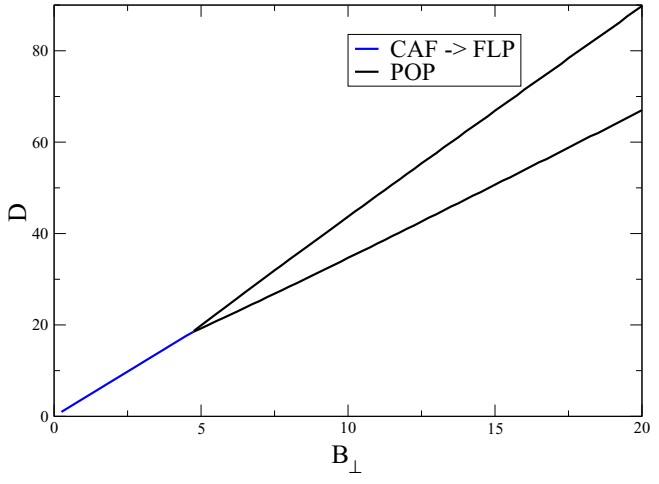

FIG. 19. Phase diagram for PS3 at an intermediate value of Zeeman coupling, $E_Z = |g_{xy}|$. This is very similar to the phase diagram of PS3 at perpendicular field. All transitions are first order.

percolate, there may be *bulk* conduction [42,43]. Thus, both first- and second-order transitions are expected to be visible in transport.

Bulk excitations can also provide information about the nature of the ground state. For example, gapless modes associated with broken U(1) symmetries should have clear signatures in heat transport [44]. Bulk excitations can also be probed via the compressibility. Several of the transitions we have described involve a U(1) symmetry breaking as the transition is crossed. In the broken-symmetry phase, near the transition where there is a soft stiffness one expects very low energy, charged merons [1]. Nevertheless, we expect the system to remain incompressible at zero temperature: in order to inject an electron, one has to combine this low-energy meron (which is expected to support a small charge) with a high-energy antimeron (carrying the remaining charge of the electron). The resulting bimeron, the form in which electrons can be injected into the system, will have nonvanishing energy in spite of the low energy of one of its components. By contrast, at a first-order transition, if the domain walls percolate we expect that electrons can be injected at arbitrarily low energy, and the system becomes compressible. At $T > 0$, the key criterion is whether the phase with spontaneously broken U(1) is below its Kosterlitz-Thouless transition temperature T_{KT}. In particular, the appearance of unbound (charged) vortices above T_{KT} may lead to singular behavior in the compressibility as a function of temperature.

Finally, layer polarizability measurements have recently become feasible for this system [25]. The level of charge in each layer continuously varies in any state for which there is a broken U(1) symmetry involving the valley degree of freedom. Thus, the FM, CAF, POP, and FLP states have a vanishing linear layer polarizability, while the $\mathrm{BU}(1)^2$, SVE, and KEK states are layer polarizable. Such experiments thus allow one to probe when the $\mathrm{U}(1)_{\mathrm{valley}}$ symmetry is spontaneously broken in the bulk.

Current experiments on BLG suggest that the CAF, FM, POP, and FLP states can be stable in BLG. In a subset of samples, at small $B_\perp$, an intermediate state [24,26] *may* have been seen between the CAF and the FLP phases, suggesting that such samples are in parameter regimes consistent with PS1 or PS2. In some samples, an intermediate phase is also seen at small $B_\perp$, albeit at large tilted field, between the FM and the FLP phases [26]. Again, this is consistent with both PS1 and PS2. In other experiments, however, no intermediate phases are seen between the CAF and the FLP at small $B_\perp$, suggesting that those samples are consistent with PS3 (Figs. 18, 19, and 20). What precisely determines in which parameter regime a particular sample might be remains unclear at this time, and is a subject for further investigation. Detailed observations at small $B_\perp$ in extremely clean and cold samples would greatly clarify the parameter regime to which pure BLG belongs.

It is interesting to carry out a thought experiment in which we assume that the bulk spin susceptibility $\frac{\partial S_z}{\partial E_Z}$ can be measured, in addition to the layer polarizability $\frac{\partial \tau_z}{\partial D}$ and the cross susceptibilities $\frac{\partial S_z}{\partial D} \equiv \frac{\partial \tau_z}{\partial E_Z}$. (The last identity is a Maxwell relation arising from $S_z = -\frac{\partial \tilde{\mathcal{E}}}{\partial E_z}$ and $\tau_z = -\frac{\partial \tilde{\mathcal{E}}}{\partial D}$.) Such measurements may indeed be accessible, e.g., using the

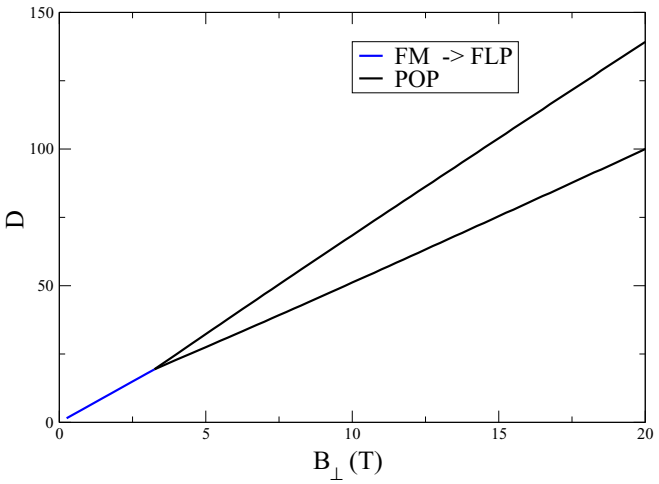

FIG. 20. Phase diagram for PS3 at a large value of Zeeman coupling $E_Z = |g_{xy}|$. The small-D phase is the FM, otherwise the phase diagram is very similar to those for PS3 at smaller E_Z.

technique of Reznikov *et al.* [45]. The combined measurement allows one to distinguish between the different possible states. The FM, CAF, POP, and FLP have a vanishing layer polarizability. The FM, KEK, and FLP have a vanishing spin susceptibility. The SVE state has both layer polarizability and spin susceptibility nonvanishing, but satisfies $S_z + \tau_z = 4$, which implies

$$\frac{\partial S_z}{\partial D} + \frac{\partial \tau_z}{\partial D} = 0 = \frac{\partial S_z}{\partial E_Z} + \frac{\partial \tau_z}{\partial E_Z}. \tag{78}$$

Finally, the BU(1)^2 state also has all susceptibilities nonvanishing, but is not subject to the condition of Eq. (78). This allows us, in principle at least, to distinguish the BU(1)^2 state from other possibilities.

B. Caveats and omissions

We next briefly review some of the underlying assumptions that lead to the model analyzed in this work. We first separated the Coulomb and other lattice scale interactions into an SU(4) symmetric part (which plays no role in choosing the ground state) and a part that does not respect SU(4) symmetry,. We assumed that the part that does not respect SU(4) symmetry can be represented as short-range interactions. These short-range interactions respect the spin SU(2) but have only a U(1) symmetry in the valley indices. Finally, we assumed that all interaction parameters g_i are proportional to $B_\perp$, corresponding to ultra-short-range interactions.

Each of these assumptions can be challenged. Consider first our assumption that $g_i \propto B_\perp$. This seems reasonable from the renormalization group (RG) standpoint, as can be seen from the following argument. At high energies, the dispersion is Dirac type, and short-range interactions are irrelevant as one scales down in energy:

$$\tilde{g}_i(\ell) = \tilde{g}_i(0)e^{-\ell}, \tag{79}$$

where $\tilde{g}_i$ are the dimensionless couplings (the ratio of the dimensionful couplings to the kinetic energy scale), ℓ is the RG flow parameter defined by $e^{-\ell} = \Lambda(\ell)/\Lambda(0)$, and $\Lambda(0)$ is the bandwidth. At a scale proportional to the interlayer hopping $t_\perp$ (corresponding to RG scale $\ell_\perp$, say), the quadratic band touching manifests itself, and the one-loop RG flow of $\tilde{g}_i$, if one neglects t_3, becomes marginal [8]. In general, the RG flows may be written in the form

$$\frac{d\tilde{g}_i}{d\ell} = C_{ijk}\tilde{g}_j\tilde{g}_k, \tag{80}$$

and should be stopped at a kinetic energy scale $\sim B_\perp$ which is of relevance to the system we are studying. Since they are marginal, the values of g_i will follow the kinetic energy scale, thus becoming proportional to $B_\perp$.

Complications arise when t_3 enters the picture. At the quadratic band touching t_3 is a relevant coupling and will grow. Further, we know that t_3 is generated by the interactions [28], and will in turn affect the flow of the g_i. Thus, it is likely that the couplings g_i do have some $B_\perp$ dependence in the presence of trigonal warping. Since we have not worked out the RG flow equations in the presence of t_3, we have not taken this into account, and have made the naive assumption that $g_i \propto B_\perp$, which follows from directly computing the interaction matrix elements for our model in the Landau levels of interest, without including any renormalization effects.

Second, we assume that all our interactions are ultra-short-range. Here, we are on somewhat firmer footing. Introducing a $\mathbf{q}$ dependence of the form $e^{-|\mathbf{q}|^2\xi^2}$ into the interactions $v_i(\mathbf{q})$ will leave the Hartree terms unchanged, but reduce the exchange terms by a factor close to unity. This does change some of the inequalities which we use to define the different parameter sets (PS1, PS2, and PS3), but does not change the qualitative nature of the phases or the topologies of the phase diagrams. As an aside, introducing such a $\mathbf{q}$ dependence into the Kharitonov model [21] will lead to a BU(1)^2 phase in the phase diagram.

Third, we reiterate that the four couplings retained in our interaction model are only a subset of many such couplings which are allowed by the symmetry of the system. This was largely to keep a tractable parameter space size for our study; however, we believe that other couplings will not qualitatively alter the topologies of the phase diagrams or the nature of the phases we encounter.

Finally, our analysis has been carried out within the Hartree-Fock approximation. Quantum fluctuations could play an important role near second-order phase transitions, particularly for states with broken U(1) symmetries. These are generically accompanied by soft stiffnesses when they are first entered, so that low-energy excitations around the HF state will necessarily exist.

VII. CONCLUSIONS AND OPEN QUESTIONS

In this work, we have studied the possible zero-temperature ground states of bilayer graphene (BLG) at charge neutrality in a quantizing perpendicular magnetic field $B_\perp$. This $\nu = 0$ system is very rich, possessing three sets of discrete labels: spin, valley, and orbital, leading to eight nearly degenerate Landau levels in the low-energy manifold. (Recall that by "low-energy manifold" we mean the manifold of states near the Fermi energy.) Experimentally, the system can be probed by applying a tilted magnetic field (to increase the Zeeman

coupling E_Z) and/or by applying a perpendicular electric field D which induces layer polarization. In the presence of these external fields, the symmetry of the problem is reduced to $\mathrm{U}(1)_{\mathrm{spin}} \times \mathrm{U}(1)_{\mathrm{valley}}$.

Our philosophy is to ignore the SU(4) symmetric, long-range part of the Coulomb interaction completely, because it plays no role in ground-state selection at $\nu = 0$. Our model is based on an effective Hamiltonian, containing only short-range interactions, in the truncated Hilbert space of the low-energy manifold. Effects of the filled Dirac sea [15–18] are assumed to be absorbed into renormalizations of the couplings of the effective Hamiltonian [20,21].

We incorporate two aspects distinct from previous work [12–14,21]: (i) We include the effect of the trigonal warping t_3 (an interlayer hopping term allowed by the lattice symmetries) nonperturbatively in the one-body states of the low-energy manifold that form our basis. (ii) In addition to interactions introduced in previous work [20,21] [g_z and g_{xy} which correspond to $\mathrm{U}(1)_{\mathrm{valley}}$ symmetric interactions], we introduce two new interactions into our effective Hamiltonian: one (g_0) which treats all discrete labels equally, and another (g_{nz}) which is an Ising-type interaction in the orbital sector.

The dependence of the dimensionless coupling constant associated with t_3 on $B_\perp$, together with suitable values of the interaction strengths, leads to the stabilization of a hitherto unknown phase. This phase, which we dub the broken $\mathrm{U}(1) \times \mathrm{U}(1)$ or $\mathrm{BU}(1)^2$ phase, spontaneously breaks two distinct U(1) symmetries, and is one of the central findings in this work. Hints of its existence can be gleaned from unexpected zero modes in the collective spectrum [29] even at $t_3 = 0$. In contrast, all phases known previously at $\nu = 0$ are either symmetric under $\mathrm{U}(1)_{\mathrm{spin}} \times \mathrm{U}(1)_{\mathrm{valley}}$ or spontaneously break a single U(1). The spin-polarized ferromagnet (FM) and the fully layer-polarized (FLP) phases are symmetric, while the canted antiferromagnet (CAF), the Kekule (KEK), and the spin-valley entangled (SVE) phases break a single U(1) symmetry.

We explored three parameter sets of couplings characterized by inequalities among them. For parameter set 1 (PS1), $g_z > g_0 + \frac{1}{2}g_{nz} + |g_{xy}|$, and the $\mathrm{BU}(1)^2$ phase invariably appears in the $B_\perp$-D phase diagram at small $B_\perp$ and small D when the **B** field is not tilted. In this regime, transitions between the CAF, $\mathrm{BU}(1)^2$, SVE, and FLP phases are driven by increasing D and are all second order. At large $B_\perp$, a partially orbitally polarized (POP) phase and the Kekule (KEK) phase intervene between the CAF and the FLP phases for intermediate values of D. Transitions between the POP and other states are always first order, while the transition from the KEK state to the FLP state is second order. As the field is tilted and the Zeeman energy increased, the $\mathrm{BU}(1)^2$ phase shrinks and disappears from the $B_\perp$-D phase diagram.

Parameter set 2 (PS2) satisfies the inequalities $g_0 + \frac{1}{2}g_{nz} + |g_{xy}| > g_z > g_0 + \frac{1}{2}g_{nz}$. In this case, the $\mathrm{BU}(1)^2$ phase, if it appears at all, is confined to a small sliver of D and $B_\perp$ near the onset of the POP state when the **B** field is untilted. At small $B_\perp$, the CAF state transitions directly to the SVE state via a first-order transition as D is increased, which in turn smoothly goes over into the FLP state via a second-order transition at even higher D. As above, at larger $B_\perp$, the POP state intervenes at intermediate D, and a KEK state may appear at higher D which ultimately gives way to the FLP state.

Parameter set 3 (PS3) satisfies $g_z < g_0 + \frac{1}{2}g_{nz}$, and has the simplest phase diagram of all. The CAF/FM state at small D undergoes a first-order transition to either the FLP or the POP state, depending on the value of $B_\perp$. All transitions in PS3 are first order.

The $\mathrm{BU}(1)^2$ phase, if it exists, always appears in a narrow window of D. Since it undergoes second-order phase transitions to states with a single broken U(1) at its D boundaries, one (pseudo)spin stiffness must always vanish at each transition. In previous work we have shown that in such cases the gap to edge transport vanishes at the transition. Depending on the details of the stiffnesses, and the temperature at which measurements are made, the $\mathrm{BU}(1)^2$ phase may appear to be metallic. An alternative possibility is that quantum fluctuations disorder at least one of the broken U(1)'s to form a symmetric phase with vanishing gap at either D boundary.

Our results also raise a host of interesting questions. Foremost among them is the issue of edge conduction in the various states. The BLG edge is expected to break all lattice symmetries, but preserve spin-rotation symmetry, because spin-orbit coupling is tiny. For the CAF state in monolayer graphene the present authors showed that edge conduction occurs via topological vortex excitations of the CAF order parameter bound to an image antivortex near the edge [32,33]. In a quantum Hall state, such topological objects carry charge due to the spin-charge relation [1]. In BLG, the SVE and KEK states are valley analogs of the CAF, and it remains to be seen whether this edge physics carries over to the two latter phases. Perhaps the most interesting is the edge $\mathrm{BU}(1)^2$ phase because the bulk supports several flavors of topological excitations [vortices can be formed from either of the two broken U(1)'s]. The effects of thermal and/or quantum disordering of the $\mathrm{BU}(1)^2$ state should also be explored.

Another set of interesting questions concerns fillings close to $\nu = 0$, particularly in the range $-4 \leqslant \nu \leqslant 4$. All these fillings nominally involve only the nearly degenerate set of Landau levels around the Fermi energy for undoped BLG. Trigonal warping likely impacts the phase diagram at such fillings, and a detailed investigation could help identify the appropriate interaction regime for BLG. Lastly, on the theoretical side, a full renormalization group analysis for the short-range couplings in the presence of t_3 and a quantizing magnetic field, while challenging, would in principle indicate the scale of couplings that apply to models such as we have analyzed, in which the degrees of freedom are projected to a small number of Landau levels.

ACKNOWLEDGMENTS

We are grateful to J. Zhu, J. Li, A. Young, M. Zaletel, and J. Ramon de Nova for illuminating conversations, and to the Aspen Center for Physics (NSF Grant No. 1066293), where this work was begun and completed. G.M. thanks the NSF (Grant No. DMR-1306897) and the Gordon and Betty Moore Foundation for financial support. H.A.F. acknowledges the support of the NSF through Grants No. DMR-1506263 and No. DMR-1506460. E.S. thanks support of the

Israel Science Foundation (ISF) via Grant No. 231/14, of the Simons Foundation, and thanks the hospitaliy of the Kavli Institute for Theoretical Physics (NSF Grant No. PHY-11-25915). Finally, we would like to acknowledge support for all the present authors by the US-Israel Binational Science Foundation (Grant No. BSF-2012120).

APPENDIX A: DERIVATION OF THE COEFFICIENTS A_{nm}

In this appendix we derive a power-series expansion in λ for the states $|\psi_A\rangle$, $|\psi_B\rangle$ [Eq. (7)], and consequently the expressions for the coefficients A_{nm} in Eq. (8). We start by considering the integral

$$\int_0^\infty dt\, e^{\frac{it^3}{3\lambda}-ita^\dagger} = \left(\frac{\lambda}{9}\right)^{1/3} e^{\frac{i\pi}{6}} \int_0^\infty d\xi\, \xi^{-2/3} e^{-\xi} \exp\left\{e^{-\frac{i\pi}{3}}(3\lambda\xi)^{1/3}a^\dagger\right\}, \tag{A1}$$

where we have used the change of variables $t^3 = i3\lambda\xi$. Implementing a power-series expansion of the last exponential factor in Eq. (A1), and performing the integration over ξ, we obtain

$$\int_0^\infty dt\, e^{\frac{it^3}{3\lambda}-ita^\dagger} = \left(\frac{\lambda}{9}\right)^{1/3} e^{\frac{i\pi}{6}} \sum_{n=0}^{\infty} \frac{(3\lambda)^{n/3}\Gamma\left(\frac{n+1}{3}\right)}{n!} e^{-\frac{in\pi}{3}} (a^\dagger)^n. \tag{A2}$$

Employing Eq. (7), we thus find

$$|\psi_A\rangle = \left(\frac{\lambda}{9}\right)^{1/3} \sum_{n=0}^{\infty} \frac{(3\lambda)^{n/3}\Gamma\left(\frac{n+1}{3}\right)}{n!} \cos\left\{\frac{\pi}{6}(2n-1)\right\}(a^\dagger)^n|0\rangle. \tag{A3}$$

To get a similar expansion for $|\psi_B\rangle$, we repeat the same steps for the purely real integral

$$\int_0^\infty dt\, e^{-\frac{t^3}{3\lambda}-ta^\dagger} = \left(\frac{\lambda}{9}\right)^{1/3} \sum_{n=0}^{\infty} \frac{(3\lambda)^{n/3}\Gamma\left(\frac{n+1}{3}\right)}{n!} (-1)^n (a^\dagger)^n\ ; \tag{A4}$$

substituting in Eq. (7), this yields

$$|\psi_B\rangle = \left(\frac{\lambda}{9}\right)^{1/3} \sum_{n=0}^{\infty} \frac{(3\lambda)^{n/3}\Gamma\left(\frac{n+1}{3}\right)}{n!} \left[(-1)^n - \sin\left\{\frac{\pi}{6}(2n-1)\right\}\right](a^\dagger)^n|0\rangle. \tag{A5}$$

We next examine the oscillating factors in Eqs. (A3) and (A5), which exhibit a threefold periodicity in n: for any integer m,

$$\begin{aligned}
&n = 3m-1 \quad \Rightarrow \quad \cos\left\{\frac{\pi}{6}(2n-1)\right\} = (-1)^n - \sin\left\{\frac{\pi}{6}(2n-1)\right\} = 0,\\
&n = 3m \quad \Rightarrow \quad \cos\left\{\frac{\pi}{6}(2n-1)\right\} = (-1)^m\frac{\sqrt{3}}{2}, \quad (-1)^n - \sin\left\{\frac{\pi}{6}(2n-1)\right\} = (-1)^m\frac{3}{2},\\
&n = 3m+1 \quad \Rightarrow \quad \cos\left\{\frac{\pi}{6}(2n-1)\right\} = (-1)^m\frac{\sqrt{3}}{2}, \quad (-1)^n - \sin\left\{\frac{\pi}{6}(2n-1)\right\} = (-1)^{m+1}\frac{3}{2}.
\end{aligned} \tag{A6}$$

Inserting Eq. (A6) in (A3) and (A5) and using $|N\rangle = \frac{1}{\sqrt{N!}}(a^\dagger)^N|0\rangle$, we obtain

$$\begin{aligned}
|\psi_A\rangle &= \frac{1}{\sqrt{3}}\left(|\tilde{\psi}_0\rangle + |\tilde{\psi}_1\rangle\right),\\
|\psi_B\rangle &= |\tilde{\psi}_0\rangle - |\tilde{\psi}_1\rangle,
\end{aligned} \tag{A7}$$

where

$$\begin{aligned}
|\tilde{\psi}_0\rangle &= \frac{(3\lambda)^{1/3}}{2} \sum_{m=0}^{\infty} (-1)^m \frac{(3\lambda)^m}{\sqrt{(3m)!}} \Gamma\left(m+\frac{1}{3}\right)|3m\rangle,\\
|\tilde{\psi}_1\rangle &= \frac{(3\lambda)^{1/3}}{2} \sum_{m=0}^{\infty} (-1)^m \frac{(3\lambda)^m}{\sqrt{(3m+1)!}} \Gamma\left(m+\frac{2}{3}\right)|3m+1\rangle.
\end{aligned} \tag{A8}$$

By definition, $|\tilde{\psi}_n\rangle$ are orthogonal ($\langle\tilde{\psi}_0|\tilde{\psi}_1\rangle = 0$) for arbitrary prefactors of each. Hence, introducing the normalization factors C_0, C_1, we arrive at the orthonormal basis states (8). Once this form has been obtained, it is straightforward to verify that these states satisfy $(a^2 + \lambda a^\dagger)|\tilde{\psi}_0\rangle = 0$.

APPENDIX B: FORM FACTORS

In this appendix, we discuss some details relevant to the calculation of the density matrix elements [Eq. (15)], and in particular how their form leads to Eq. (20). We begin with the basis states $|n,\alpha,k\rangle$ in Eq. (9):

$$|n,\alpha,k\rangle \equiv \sum_{m=0}^{\infty}(-1)^{m\alpha}A_{nm}|3m+n,k\rangle, \tag{B1}$$

for which the coefficients A_{nm} are defined in Eq. (8). Direct substitution yields the explicit form

$$\tilde{\rho}^{\alpha\beta}_{n_1n_2}(\mathbf{q}) = \sum_{k_1=0}^{\infty}\sum_{k_2=0}^{\infty}(-1)^{k_1\alpha+k_2\beta}A_{n_1k_1}A_{n_2k_2}\rho_{3k_1+n_1,3k_2+n_2}(\mathbf{q}), \tag{B2}$$

where the usual Landau level matrix elements are defined as

$$\rho_{n_1n_2}(\mathbf{q}) = (-1)^{n_<+n_2}e^{-q^2\ell^2/4}\sqrt{\frac{n_<!}{n_>!}}\,e^{i(n_1-n_2)(\theta_q-\pi/2)}\left(\frac{q\ell}{\sqrt{2}}\right)^{n_>-n_<}L_{n_<}^{|n_1-n_2|}\left(\frac{q^2\ell^2}{2}\right). \tag{B3}$$

In this equation, $n_<$ ($n_>$) is the smaller (larger) of n_1 and n_2, L_m^n is an associated Laguerre polynomial, and θ_q is the angle formed by $\mathbf{q}$ with the $\hat{x}$ axis. Now, consider the exchange integral

$$\begin{aligned}&\int\frac{d^2q}{(2\pi)^2}v(\mathbf{q})\tilde{\rho}^{\alpha\beta}_{n_1n_2}(\mathbf{q})\tilde{\rho}^{\gamma\delta}_{m_1m_2}(-\mathbf{q})\\ &\quad=\sum_{k_1k_2k_3k_4}(-1)^{k_1\alpha+k_2\beta+k_3\gamma+k_4\delta}A_{n_1k_1}A_{n_2k_2}A_{m_1k_3}A_{m_2k_4}\int\frac{d^2q}{(2\pi)^2}v(\mathbf{q})\rho_{3k_1+n_1,3k_2+n_2}(\mathbf{q})\rho_{3k_3+m_1,3k_4+m_2}(-\mathbf{q}).\end{aligned} \tag{B4}$$

Writing $N_1 \equiv 3k_1+n_1$, $N_2 \equiv 3k_2+n_2$, $M_1 \equiv 3k_3+m_1$, and $M_2 \equiv 3k_4+m_2$, Eq. (B4) can be reexpressed as

$$\begin{aligned}\int\frac{d^2q}{(2\pi)^2}v(\mathbf{q})\tilde{\rho}^{\alpha\beta}_{n_1n_2}(\mathbf{q})\tilde{\rho}^{\gamma\delta}_{m_1m_2}(-\mathbf{q}) &= \sum_{k_1k_2k_3k_4}(-1)^{k_1\alpha+k_2\beta+k_3\gamma+k_4\delta}A_{n_1k_1}A_{n_2k_2}A_{m_1k_3}A_{m_2k_4}\\ &\times\int\frac{d^2q}{(2\pi)^2}v(\mathbf{q})e^{-q^2\ell^2/2}(-1)^{N_<+N_2+M_<+M_2+M_1+M_2}\sqrt{\frac{N_<!M_<!}{N_>!M_>!}}\,e^{i(\theta_1-\frac{\pi}{2})(N_1-N_2+M_1-M_2)}\\ &\times\left(\frac{q\ell}{\sqrt{2}}\right)^{|N_1-N_2|+|M_1-M_2|}L_{N_<}^{|N_1-N_2|}\left(\frac{q^2\ell^2}{2}\right)L_{M_<}^{|M_1-M_2|}\left(\frac{q^2\ell^2}{2}\right),\end{aligned} \tag{B5}$$

where we used the property

$$\rho_{n_1n_2}(-\mathbf{q}) = (-1)^{n_1+n_2}\rho_{n_1n_2}(\mathbf{q}).$$

The integration over θ_q forces the integral to vanish unless $N_1+M_1 = N_2+M_2$. Moreover, specializing to the case where $v(\mathbf{q})$ has no $\mathbf{q}$ dependence, the orthogonality relation

$$\int_0^{\infty}dx\,e^{-x}x^{\alpha}L_m^{\alpha}(x)L_n^{\alpha}(x) = \frac{\Gamma(n+\alpha+1)}{n!}\delta_{mn} \tag{B6}$$

guarantees that the integral in Eq. (B5) vanishes unless $N_< = M_<$. Writing $v(\mathbf{q}) \to \tilde{v}$, we arrive at the relation

$$\int\frac{d^2q}{(2\pi)^2}v(\mathbf{q})\tilde{\rho}^{\alpha\beta}_{n_1n_2}(\mathbf{q})\tilde{\rho}^{\gamma\delta}_{m_1m_2}(-\mathbf{q}) = \frac{\tilde{v}}{2\pi\ell^2}\delta_{n_1m_2}\delta_{m_1n_2}r^{(n_1)}_{\alpha\delta}r^{(n_2)}_{\beta\gamma}, \tag{B7}$$

where

$$r^{(n)}_{\alpha\beta} = \sum_{k=0}^{\infty}(-1)^{k(\alpha+\beta)}A^2_{nk} \equiv \delta_{\alpha\beta}+r(1-\delta_{\alpha\beta}). \tag{B8}$$

$r^{(n)}_{\alpha\beta}$ turns out to be unity if $\alpha=\beta$ because of the normalization condition that the wave function's coefficients A_{nk} must obey. For $\alpha\neq\beta$, the sum is nontrivial, but we have found by direct summation that its value is the *same* for both values of n to within any numerical accuracy we can attain. For this reason, the quantity

$$r = \sum_{k=0}^{\infty}(-1)^kA^2_{nk}$$

is for all intents and purposes independent of n. Equation (B8) yields the result used in Eq. (20).

[1] S. M. Girvin and A. H. MacDonald, in *Perspectives in Quantum Hall Effects*, edited by S. Das Sarma and A. Pinczuk (Wiley, New York, 1997); D. H. Lee and C. L. Kane, Phys. Rev. Lett. **64**, 1313 (1990); S. L. Sondhi, A. Karlhede, S. A. Kivelson, and E. H. Rezayi, Phys. Rev. B **47**, 16419 (1993); K. Moon, H. Mori, K. Yang, S. M. Girvin, A. H. MacDonald, L. Zheng, D. Yoshioka, and S.-C. Zhang, *ibid.* **51**, 5138 (1995).

[2] V. P. Gusynin and S. G. Sharapov, Phys. Rev. Lett. **95**, 146801 (2005).

[3] E. McCann and V.I. Falko, Phys. Rev. Lett. **96**, 086805 (2006).

[4] K. Yang, S. Das Sarma, and A. H. MacDonald, Phys. Rev. B **74**, 075423 (2006).

[5] R. Nandkishore and L. Levitov, Phys. Rev. Lett. **104**, 156803 (2010); Phys. Rev. B **82**, 115431 (2010).

[6] O. Vafek and K. Yang, Phys. Rev. B **81**, 041401 (2010).

[7] F. Zhang, H. Min, M. Polini, and A. H. MacDonald, Phys. Rev. B **81**, 041402 (2010).

[8] O. Vafek, Phys. Rev. B **82**, 205106 (2010).

[9] Y. Barlas, R. Cote, K. Nomura, and A. H. MacDonald, Phys. Rev. Lett. **101**, 097601 (2008).

[10] E. V. Gorbar, V. P. Gusynin, J. Jia, and V. A. Miransky, Phys. Rev. B **84**, 235449 (2011).

[11] J. Lambert and R. Côté, Phys. Rev. B **87**, 115415 (2013).

[12] V. Lukose and R. Shankar, Phys. Rev. B **94**, 085135 (2016).

[13] A. Knothe and T. Jolicoeur, Phys. Rev. B **94**, 235149 (2016).

[14] J. Jia, P. K. Pyatkovskiy, E. V. Gorbar, and V. P. Gusynin, Phys. Rev. B **95**, 045410 (2017).

[15] I. F. Herbut, Phys. Rev. B **75**, 165411 (2007).

[16] K. Shizuya, Phys. Rev. B **86**, 045431 (2012).

[17] B. Roy, Phys. Rev. B **89**, 201401 (2014).

[18] B. Roy, M. P. Kennett, and S. Das Sarma, Phys. Rev. B **90**, 201409 (2014).

[19] B. Feshami and H. A. Fertig, Phys. Rev. B **94**, 245435 (2016).

[20] M. Kharitonov, Phys. Rev. B **85**, 155439 (2012).

[21] M. Kharitonov, Phys. Rev. Lett. **109**, 046803 (2012).

[22] R. T. Weitz, M. T. Allen, B. E. Feldman, J. Martin, and A. Yacoby, Science **330**, 812 (2010).

[23] J. Velasco *et al.*, Nat. Nanotechnol. **7**, 156 (2012).

[24] P. Maher, C. R. Dean, A. F. Young, T. Taniguchi, K. Watanabe, K. L. Shepard, J. Hone, and P. Kim, Nat. Phys. **9**, 154 (2013).

[25] B. M. Hunt, J. I. A. Li, A. A. Zibrov, L. Wang, T. Taniguchi, K. Watanabe, J. Hone, C. R. Dean, M. Zaletel, R. C. Ashoori, and A. F. Young, Nat. Commun. **8**, 948 (2017).

[26] J. Zhu (private communication).

[27] J. Jung and A.H. MacDonald, Phys. Rev. B **89**, 035405 (2014).

[28] S. Pujari, T. C. Lang, G. Murthy, and R. K. Kaul, Phys. Rev. Lett. **117**, 086404 (2016).

[29] J. R. M. de Nova and I. Zapata, Phys. Rev. B **95**, 165427 (2017).

[30] A. B. Kuzmenko, I. Crassee, D. van der Marel, P. Blake, and K. S. Novoselov, Phys. Rev. B **80**, 165406 (2009).

[31] *Handbook of Mathematical Functions*, edited by M. Abramowitz and I. A. Stegun (National Bureau of Standards, United States Department of Commerce, 1964).

[32] G. Murthy, E. Shimshoni, and H. A. Fertig, Phys. Rev. B **90**, 241410 (2014).

[33] G. Murthy, E. Shimshoni, and H. A. Fertig, Phys. Rev. B **93**, 045105 (2016).

[34] T. Jungwirth and A. H. MacDonald, Phys. Rev. B **63**, 035305 (2000).

[35] J. Li, Y. Tupikov, K. Watanabe, Takashi Taniguchi, and Jun Zhu, arXiv:1708.03644.

[36] D. A. Abanin, P. A. Lee, and L. S. Levitov, Phys. Rev. Lett. **96**, 176803 (2006).

[37] H. A. Fertig and L. Brey, Phys. Rev. Lett. **97**, 116805 (2006).

[38] E. Shimshoni, H. A. Fertig, and G. V. Pai, Phys. Rev. Lett. **102**, 206408 (2009).

[39] P. Tikhonov, E. Shimshoni, H. A. Fertig, and G. Murthy, Phys. Rev. B **93**, 115137 (2016).

[40] M. Kharitonov, Phys. Rev. B **86**, 075450 (2012).

[41] M. Kharitonov, S. Juergens, and B. Trauzettel, Phys. Rev. B **94**, 035146 (2016).

[42] T. Jungwirth and A. H. MacDonald, Phys. Rev. Lett. **87**, 216801 (2001).

[43] K. Dhochak, E. Shimshoni, and E. Berg, Phys. Rev. B **91**, 165107 (2015).

[44] F. Pientka, J. Waissman, P. Kim, and B. I. Halperin, Phys. Rev. Lett. **119**, 027601 (2017).

[45] M. Reznikov, A. Yu. Kuntsevich, N. Teneh, and V. M. Pudalov, JETP Lett. **92**, 470 (2010); N. Teneh, A. Yu. Kuntsevich, V. M. Pudalov, and M. Reznikov, Phys. Rev. Lett. **109**, 226403 (2012).